PETROLOGICAL AND GEOCHEMICAL EVIDENCE FOR PUTATIVE ANCIENT MICROFOSSILS WITHIN THE BERLINS PORPHYRY, NEW ZEALAND

A THESIS SUBMITTED IN

PARTIAL FULFILLMENT OF THE REQUIREMENTS FOR

THE DEGREE OF

MASTER OF SCIENCE IN GEOLOGY

AT THE UNIVERSITY OF CANTERBURY

BY TONI LOUISE COX

UNIVERSITY OF CANTERBURY

UNIVERSITY OF CANTERBURY
Te Whare Wānanga o Waitaha
CHRISTCHURCH NEW ZEALAND

2013

“Life is Only the Beginning” – Joseph Conrad

Abstract

Berlins Porphyry, located on the South Island of New Zealand, is the result of granitic intrusions, brecciation and hydrothermal alteration of country rock. Exposure of the Berlins Porphyry provides an opportunity to examine high temperature hydrothermal systems at depth (~2km) and to investigate the potential of biological activity in areas of localized hydrothermal activity. All Berlins Porphyry deposits are mineralogically and geochemically similar; however, localized areas within the porphyry show increased hydrothermal activity. Locations for microbial investigations include outer porphyry alteration zones that experienced high levels of hydrothermal fluid alteration. A recently exposed and highly altered porphyry outcrop on the Denniston Plateau contains iron concretions generated during localized hydrothermal mineralization. Here we show the Fe-rich concretions are the result of biomineralization via crystal morphology observations, carbon chemistry analysis and putative microfossils. High resolution petrographic and cathodoluminescence imaging reveals a variety of ancient fossilized burrows present within the magnetite zone. Transects through the concretions demonstrate that the abundance of carbon increases in the magnetite zone and exhibits $\delta^{13}C‰$ values characteristic of organic carbon (averaging -26‰ ± 4‰). Alteration mineralogy including recrystallized quartz, muscovite, adularia and kaolinite are present within the Berlins Porphyry iron concretions and suggest a hydrothermal system with microbial activity operating at temperatures between 200-250°C. Overall, these ancient and unusually persevered microbially-mediated Fe-rich concretions potentially represent a significant temperature increase for the habitability of life.

Acknowledgements

I would like to first and foremost thank my supervisor, Dr. Chris Oze for his astounding knowledge and enthusiasm towards our research. His guidance, discussions, patience and willingness to support all aspects of my post graduate degree made my time at the University of Canterbury both exciting and unforgettable.

I am indebted to Dr. Travis Horton for his role in our research, without his expertise on carbon isotopes we would not have confirmed life was present within the Berlins Porphyry. His enthusiasm and charismatic attitude only added to the excitement of this project.

Thank you to Dr. Anekant Wandres for his amazing GIS skills and his guidance through the Cretaceous geology of the Lower Buller Gorge and the Denniston Plateau.

Big thank you to the Department of Geological Science for funding over the summer to kick start my thesis and Mason Trust Fund, without I would not have been able to complete my fieldwork and geochemical analysis.

Thank you Solid Energy, in particular John Taylor, Gayla Bonham-Carter and Stuart Henley for their guidance in the field and allocation of core samples. To Buller Coal for their generous supply of core samples and to Simon Nathan (GNS), John Bradshaw (University of Canterbury), Paul Wopereis (MWH) and John Gurney (Denniston Experience) for their local geological knowledge of the Lower Buller Gorge and Denniston Plateau.

Thank you GNS Dunedin and University of Otago, specifically Rose Turnbull, Andreas Auer, David Prior and Andy Tullock for their help and direction throughout my stay in Dunedin.

I am indebted to Rob Spiers for his time and expertise in the making of over 40 thin sections and to Dr. Kerry Swanson for his patience using the SEM and petrographic microscopes and for his wisdom on ancient bacteria.

I would like to show my gratitude to the department's administration and technical staff (Pat Roberts, Janet Warburton, Chris Grimshaw, Sacha Baldwin-Cunningham, Cathy Higgins, Vanessa Tappenden, John Southward and Stephen Brown) for all their work and support throughout my research.

I am grateful to Lauren Foote for her complete generosity as a field assistant and for always keeping me on track, to Quinten van der Meer for his sledge hammer assistance in the field, to Florence Begue and Kari Basset for their time and expertise using the CL-SEM and to Jacqueline Dohaney for her support in both my petrological analysis and visual presentation skills.

I would like to thank my partner Mike Jeffcott who remained in Christchurch so I could complete my Masters and for his unconditional support, patience and reassurance over the last few years. To Sarah Bastin and all my close friends for being there during the hard yards and offering well needed distractions over the years.

Lastly, thank you to my entire family for their patience and support over the years and a special thanks to my Mum, Jutka Cox for her devotion and encouragement towards me living my dream.

Table of Contents

List of Figures and Tables

Chapter Two

Chapter Three

Chapter Four

Chapter Five

Abbreviations and Acronyms

Bt – Biotite

Cal – Calcite

Chl – Chlorite

CL – Cathodoluminescence

DP – Denniston Plateau

EDS – Energy Dispersive Spectroscopy

EM –Electron Microprobe

EMORB – Enriched Mid-Ocean Ridge Basalt

GNS – Geological and Nuclear Science

Hm – Hematite

HREE – Heavy Rare Earth Elements

Kal – Kaolinite

Ksp – Alkali Feldspar

LBG – Lower Buller Gorge

LC – Living Cavity

LREE – Light Rare Earth Elements

Ma – Millions of Years

Mg – Magnetite

MORB – Mid-Ocean Ridge Basalt

Msc – Muscovite

NMORB – Normal Mid-Ocean Ridge Basalt

OIB – Ocean Island Basalt

Plg – Plagioclase Feldspar

PPL – Plane Polarized Light

Qtz – Quartz

REE – Rare Earth Elements

SEI – Scanning Electron Image

SEM – Scanning Electron Microscopy

UC – Unconformity

WDS – Wavelength Dispersive X-ray Spectroscopy

wt% – Weight Percentage

XPL – Crossed Polarized Light

XRD – X-Ray Diffraction

Xt – Xenolith

Chapter One – Introduction

1.1 Overview

Porphyry systems are located in the upper and outer zones of magmatic chambers, where high temperatures, pressures and hydrothermal fluids generate extensive alteration (Gustafson, 1975; Hendenquist & Lowenstern, 1994; Sillitoe, 2010). These systems are associated with convergent volcanic arcs and result through the interaction of large granitic intrusives with surrounding country rock and migrating fluids (Hedenquist & Lowenstern, 1994; Candela, 1997). The granitic intrusions and related country rock interact with hydrothermal fluids and are metasomatised causing the alteration and dissolution of primary minerals and formation of secondary minerals (Sillitoe, 1972; Hendenquist & Lowenstern, 1994; Xue et al. 2012). As a result, the original composition of the rock is overprinted, erased and/or replaced with hydrothermal mineralization (GACMDD, 1996) making it difficult to preserve or evaluate these processes until they reach the surface.

Previous research on porphyry systems concentrate on hydrothermal ore mineralization (e.g., Sillitoe, 1972; Gustafson, 1975; Hedenquist & Lowenstern, 1994; Candela, 1997; Sillitoe, 2010; Xue et al. 2012), while broader alteration zones not associated with economic resources are overlooked. Porphyry deposits that contain no sulphides or metal ore are poorly understood as they are not significant in mineral investigations. Further geological investigations of unprofitable porphyry systems are limited, therefore the potential for these environments to host microbial activity is unknown. Shallow hydrothermal systems have previously shown they possess the required conditions to sustain life (e.g. Juniper & Fouquet, 1988; Rasmussen, 2000; Al-Hanbali & Holm, 2002; Amend et al. 2003), but deep-seated hydrothermal systems have yet to show evidence of microbial activity. Although these deep-seated hydrothermal environments are typically viewed as unstable, they possess a constant supply of mineral enriched fluids, which many “extreme” living systems depend on (Hendenquist & Lowenstern, 1994; Templeton, 2011).

New Zealand's Berlins Porphyry is comprised of a variety of intermediate, granodioritic to dacitic plutons (Nathan, 1974) that intrude at shallow depths (~2km) through the Lower Buller Gorge (LBG) and Denniston Plateau (DP); (Fig. 2.1). Despite Nathan (1974) suggesting that all Berlins Porphyry intrusions are geochemically homogenous, variations in the intrusion sizes, shapes, composition, and texture suggest the intrusions may exhibit geochemical variations. Additionally, the age of Berlins Porphyry, its alteration history and the presence of large overlying unconformities affect the homogeneity of the intrusions. The Berlins porphyry shows no substantial economic wealth; however, its rare exposure and preservation allows the opportunity to examine these high temperature hydrothermal systems at depth and to investigate the potential of biological activity in these environments. This study aims to re-examine the Berlins Porphyry deposits and search for potential sites where microbial activity at depths can be examined. Such locations include recently exposed and localized hydrothermally altered deposits towards the outer alteration zones of the Berlins Porphyry.

1.2 Research Objectives and Agenda

The objectives of this research are to:

- Re-characterise the Berlins Porphyry, confirming that the location of all previously mapped deposits in the Lower Buller Gorge and Denniston Plateau are related.
- Evaluate the highly altered unit of the Berlins Porphyry on the Denniston Plateau, specifically focusing on the potential for biologically induced mineralization as a formation mechanism for the Fe-rich concretions.

This thesis presents a comprehensive geologic and biologic overview in Chapter 2, describing the geology and Cretaceous evolution of the Westland region. Additionally, Chapter 2 reviews current research on microbial processes within geological environments and includes current criteria for identifying microfossils within crystalline rocks.

Chapter 3 details the methods of this research, including field sampling, mineralogical and geochemical analysis, and carbon isotope chemistry.

Chapter 4 presents the results of field sampling, petrographic analysis, electron microscopy (EM), scanning electron microscopy with energy dispersive X-ray (SEM-EDS) and cathodoluminescence (CL) capabilities, X-ray diffraction analysis (XRD), whole rock analysis and carbon isotope chemistry.

Chapter 5 proposes a model for the emplacement of the Berlins Porphyry intrusions, based on mineralogical, textural and geochemical interpretations. A discussion of the alteration within the Berlins Porphyry and the potential for the presence of microbial life is presented. The overall implications for microfossils residing in deep-seated and high temperature ancient hydrothermal systems are discussed.

Chapter 6 summarises the results and interpretations presented in Chapters 2 to 5, and provides overall conclusions for this research.

Chapter Two – Geological and Biological Review

2.1 Geology of the Berlins Porphyry

Berlins Porphyry or Berlins Quartz Porphyry deposits are 111 ± 2Ma (U-Pb) granodioritic intrusions that outcrop discontinuously throughout the Lower Buller Gorge (LBG) and the Denniston Plateau (DP) of New Zealand (Nathan, 1974; Muir et al.1997).

The intrusions range in size from 3 meters to 2 kilometers in width (Muir et al. 1997) and display zoning from a porphyritic hyalodacite to a microgranodiorite and a coarse grained granodioritic centre (Nathan, 1974). The unaltered porphyry (Fig. 2.1 A) hosts characteristic resorbed quartz crystals and euhedral or broken plagioclase feldspar and biotite crystals (Nathan, 1974). High percentages of plagioclase feldspar (20-25%) and biotite (10-15%) contribute to the intermediate composition of the Berlins Porphyry. Accessory mineralogy includes alkali feldspar, chlorite, magnetite, pyrite, Greenland Group basement xenoliths and volcanic glass (Nathan, 1974). The main variation between the hyalodacite and the granodiorite is the texture; the hyalodacite displays broken phenocrysts in a glassy/fragmented crystalline groundmass and the granodiorite contains euhedral, interlocking crystals with no groundmass.

The history of alteration within the Berlins Porphyry is complex due to large regional unconformities, a product of regional tectonics and erosion. These unconformities vary from ~10Ma in the LBG to ~70Ma on the DP (Fig. 2.2).

Hydrothermal alteration (Nathan et al. 2002) and weathering is evident in both of these locations, however, determining which type of alteration is difficult in the field. The formation of the highly altered porphyry on the plateau (Fig. 2.1 B) can only be elucidated through mineralogical changes.

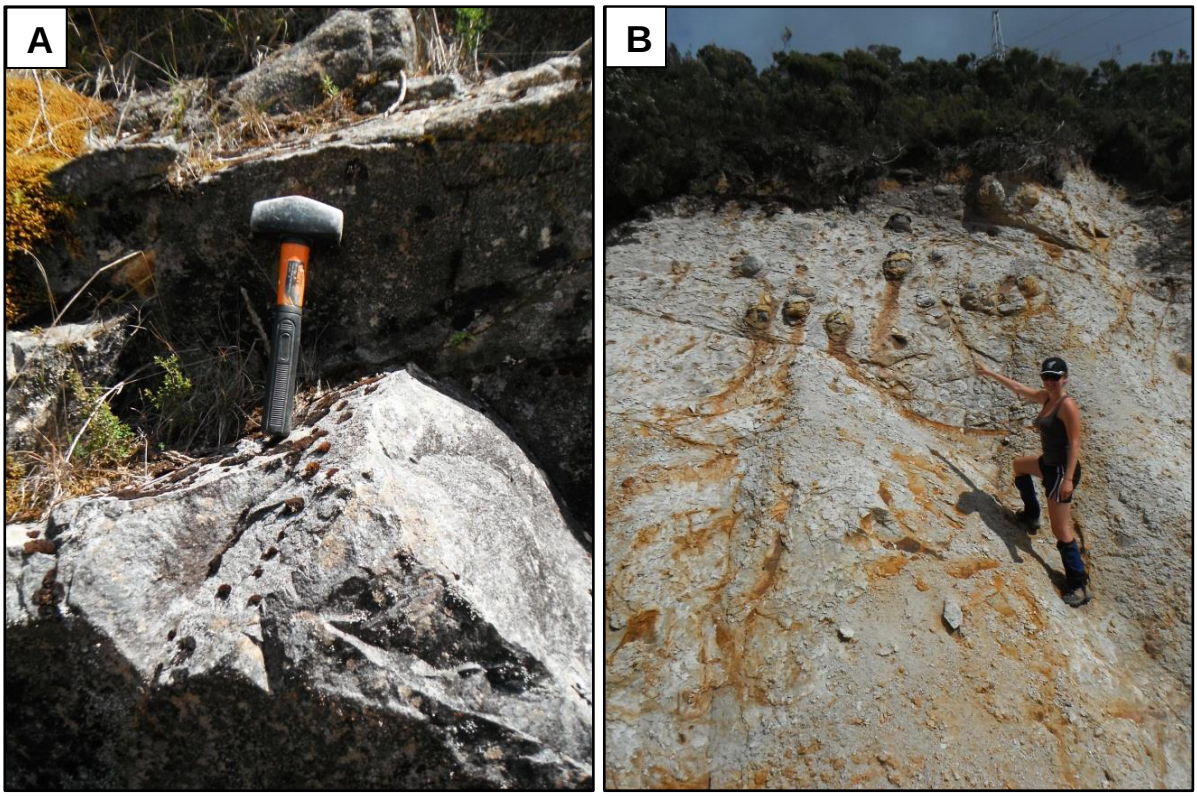

Figure 2.1: These field photographs display the variability within the Berlins Porphyry on the Denniston Plateau. Photograph (A) shows an unaltered dark grey porphyry outcrop and photograph (B) displays an intensely altered white and iron-stained porphyry outcrop with Fe-rich boulder-like structures.

2.2 Geologic Evolution of the Lower Buller Gorge and Denniston Plateau

New Zealand's South Island is comprised of two provinces; a Western and Eastern province. The Berlins Porphyry of the Western province intrudes the Greenland Group basement rock (Fig. 2.2), commonly incorporating metamorphosed host rock xenoliths within its margins (Nathan, 1974). The Stitts Tuffs, Hawks Crag Breccia and Brunner Coal Measures rest unconformably above the Berlins Porphyry (Muir et al. 1997; Fig. 2.2). The Stitts Tuffs were previously suggested to be surface volcanic deposits, accompanying the shallow Berlins Porphyry emplacement (Adams & Nathan, 1978). After U-Pb dating by Muir et al. (1997) a time gap of ~10 million years separated the two lithologies. This concluded that the Stitts Tuffs (101 ± 2 Ma) are not an extrusive equivalent of the Berlins Porphyry (111 ± 2 Ma; Muir et al. 1997), but instead a later volcanic event.

Cretaceous calc-alkaline granitoids of the Western Province magmatically link through crystallization correlations between the Berlins Porphyry and the Buckland Granite (Waight, 1995; Muir et al. 1997). Geochronological evidence indicates these calc-alkaline granites intruded contemporaneous with regional uplift and erosion over 115 – 95 million years ago (Adams & Nathan, 1978; Spell et al. 2000). This regions uplift is attributed to large scale crustal extension of the New Zealand continent, evident from core complexes forming in the Eastern and Western provinces (between 140-110Ma); (Gibson et al. 1988; Spell et al. 2000; Forster & Lister, 2003). The formation of the core complexes, in particular the Paparoa core complex, amplified heat flow in the region and contributed to the emplacement of the granitoids. This extension predates the demise of the subduction system (105 ± 5 Ma) along the Panthalassen Gondwana margin (Wandres & Bradshaw, 2005).

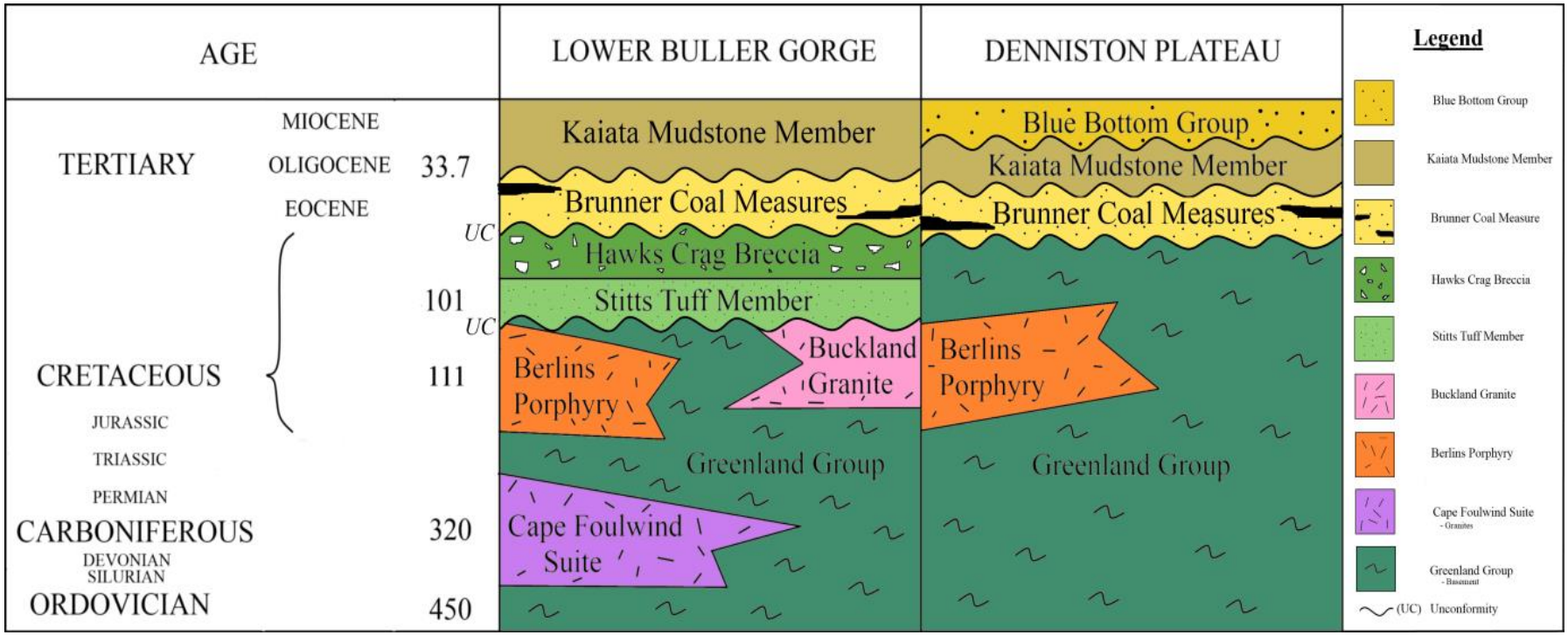

Figure 2.2: A simplified stratigraphic column displaying rock units present in the LBG and on the DP. Greenland Group ages are derived from Adams (2004) and Stitts Tuff and the Berlins Porphyry's age is from Muir et al. (1997). The general ages of Cenozoic sedimentary sequences are from Nathan et al. (1986).

2.3 Microbial Activity in Hydrothermal Systems

The nature and role of microorganisms, specifically chemo-autotrophs within geologic systems, vary based on the environmental conditions at each location. A chemo-autotroph can be clarified through its name; 'auto' is Greek for "one's own", 'troph' signifies "nutritive" and 'chemo' suggests chemical. A chemo-auto-troph is therefore, an organism that utilizes chemicals for its own nutrients.

Chemo-autotrophs have been discovered residing within weathering systems (e.g., Wierzchos et al. 2003; Rong et al. 2008; Uroz et al. 2009), volcanic systems (e.g., Thorseth et al. 1992; Peckmann et al. 2008; Staudigel et al. 2008; Ivarsson et al. 2011; Templeton, 2011), and modern/ancient hydrothermal systems (e.g., Juniper & Fouquet, 1988; Pedersen, 1997; Stetter, 1999; Rasmussen, 2000; Al-Hanbali & Holm, 2002; Amend et al. 2003; Edwards et al. 2011). Each environment provides the chemo-autotroph with sustainable energy in the form of chemical reactions and the alteration of minerals.

Geologic systems such as deep sea hydrothermal vents, seafloor basalts, deep-seated igneous and metamorphic aquifers, hydrothermal pools, acid mine drainage, and frozen lakes host a specific type of chemo-autotroph referred to as extremophiles (Brack & Pillinger, 1998; Stetter, 1999; Pedersen, 2000; Thorseth et al. 2001; Kashefi & Lovely, 2003; Ivarsson et al. 2008; Templeton, 2011). These microorganisms withstand harsh environmental conditions such as exceedingly high/low temperatures, high pressures, limited light, high acidity, high alkalinity, low water concentrations, and/or low organic content (Stetter, 1999; Templeton, 2011).

Modern extremophiles are recorded surviving at 5 km depth within the crust, inside igneous rock aquifers (Pedersen, 2000). These microorganisms migrate from the surface through permeable pathways and colonize the aquifers. The highest temperature modern extremophiles have been discovered in is 121°C, found at deep sea hydrothermal vents (Kashefi & Lovely, 2003). These microorganisms are classified as hyper-thermophiles, surviving in temperatures >80°C. The closest temperature relative is *Pyrolobus fumarii* living at 113°C (Stetter, 1999) and is also found at a deep sea hydrothermal vent. These vents are common locations for hyper-thermophiles to colonize as they possess a continuous supply of mineral enriched fluids.

Chemo-autotrophs at hydrothermal vents have the ability to induce the transfer of electrons, dissolve minerals and mediate mineral precipitation (Lowenstam, 1981; Ferris et al. 1986). They can act as catalysts in chemical and mineralogical reactions, whilst utilizing energy produced from the electron transfer (Bach & Edwards, 2003). For example, iron oxidising bacteria can oxidise dissolved Fe^{2+} to a more insoluble Fe^{3+} and drive the precipitation of iron oxides and oxyhydroxides (Roden et al. 2004; Edwards et al. 2011). These types of reactions can also produce significant amounts of H_2, a principal electron donor for anaerobic microbial metabolism (Jannasch & Mottl, 1985).

The Berlins Porphyry is an exposed ancient deep-seated hydrothermal system. These systems experience temperatures from 200-800°C, are found at depths of 2-15km and their pH varies considerably (Nathan, 1974; Sillitoe, 2010). The potential for life in these systems has not previously been investigated.

2.4 Identifying Microfossils within Crystalline Rocks

Identifying and interpreting fossilized microorganisms within ancient rocks is difficult as time has a way of erasing biomarkers. Microfossil identifications must therefore be based on a set of standard biologic and geologic criteria. A set of six criterion has been developed to verify microfossils are biogenic in origin (Schopf & Walter, 1983; Buick, 1990; Gibson et al. 2001; Ivarsson, 2006). These six criteria are discussed below.

Geological Context

A comprehensive understanding of the rock the microbes reside within is required before any biological investigations begin; this should include the host rock's age and geological history. The likelihood of the host rock containing microorganisms during its formation must also be addressed. This involves investigating previous temperatures, pressures and pH of the ancient hydrothermal system, and possible energy sources available for the microorganisms.

Microfossil Morphology

Any biological structures within a host rock should exhibit typical microbial morphologies. Three common morphologies of microfossils include spherical structures, vermicular tubules and

segmented/branching filaments (Thorseth et al. 2001; Ivarsson et al. 2008; Peckmann et al. 2008; Sahl et al. 2008). These microfossils are typically in the order of tens of microns in size.

Biogenic Features and Organic Carbon Signatures

Biogenic features such as cell wall material or segmented septae can directly confirm a structure is biogenic in origin (Ivarsson, 2006). An organic carbon signature is a sufficient alternative to confirm a structure is organic (Bach & Edwards, 2003).

Microfossils Source

An investigation into whether the microfossils are indigenous to the host rock or modern contaminants is required. For example, a weathered granite sample may host microfossils sourced from a late-stage weathering process. Additionally, a hydrothermally altered rock may host microfossils that are indigenous to the alteration event. In this case, the alteration mineralogy must interact with the microfossils, biomineralization or other biomarkers within the rock (Ivarsson, 2006).

Biomineralization

The presence of biomineralization can indicate whether a microorganism is interacting with the host rock or geologic system. Biomineralization can occur as a range of mineralogy, but is often texturally distinct from the inorganic equivalents. For example, biomineralized magnetite crystals are typically sub-rounded cubic, hexagonal or bullet-like shapes (Kirschvink & Lowenstam, 1979; Mann et al. 1984; Chang & Kirschvink, 1989; Sparks et al. 1990), whilst inorganic magnetite crystals are prismatic with sharp angular edges (Davis, 1976; Heider & Dunlop, 1987; Heider, 1987).

Two types of biomineralization exist, intracellular and extracellular crystallization (i.e., internally or externally precipitated mineralization; Sparks et al. 1990). A study of marine magnetotactic bacterium by Sparks et al. (1990) highlights intracellular magnetite crystals are typically uniform in size, morphologically specific, and of high structural perfection. In comparison, extracellular magnetite crystals display irregular shapes, sizes, and contain no evidence of cellular material.

Colony/Community Evidence

Microorganisms typically live in colonies providing them with an advantage over solitary microorganisms when harnessing energy. These colonies or communities are displayed as genetically identical clusters or as biofilms of numerous species (Templeton & Knowles, 2009).

Variations to the set of six criteria have been successfully utilized in a variety of microbial studies (e.g., Awramik et al. 1983; Trewin & Knoll, 1999; Gibson et al. 2001; Al-Hanbali & Holm, 2002; Ivarsson et al. 2008; Eickmann et al. 2009); however, gaining the evidence required for all six criteria is challenging and not always possible. These criteria will serve for identifying the presence of microfossils within the Berlins Porphyry.

Chapter Three – Methods and Materials

3.1 Field Sampling

Berlins Porphyry samples were collected from the Lower Buller Gorge (LBG) and the Denniston Plateau (DP), New Zealand (Fig. 3.1). Six sample sites (Table 3.1) were selected based on their accessibility and even dispersal over the large field area. Fifteen outcrops were then sampled across the six sites (Fig. 3.1; Table 3.2) and collected from 10cm into the outcrop to avoid weathered surfaces. Field photos of the outcrops sampled are included in the Appendix. Certain sites in the LBG that were previously sampled by Nathan (1974) were inaccessible and only thin sections of these samples were available from GNS for analysis. Basement rock core samples from the Denniston Plateau were supplied by Buller Coal (core 1) and Solid Energy (core 2).

Table 3.1: Field observations of each sampling sites and core samples

Field Sampling Site	Field Description
Site 1	A series of outcrops on an electricity service road near Mackley River. Sites 1A & C were heavily weathered and Sites 1B & D were blocky and heavily jointed outcrops hosting boulder-like structures within the porphyry.
Site 2	A small outcrop along Conns Creek, near Waimangaroa River. Samples were heavily weathered and not in situ, therefore not used for analysis.
Site 3	A series of diverse outcrops on the Denniston Plateau. Sites 3A & B were heavily altered porphyry and abundant in Fe-rich boulder-like structures (3-50cm diameters). Sites 3C & D are grey and unaltered porphyry samples.
Site 4	A series of outcrops on the Lower Buller Gorge Road and southern Buller River bank. Site 4A was heavily weathered, Site 4B hosted grey-pink porphyry and Site 4C was situated on the Buller River bank and weathered.
Site 5	A small grey-green porphyry outcrop on the Denniston Plateau Mount Williams Track, at 900m elevation.
Site 6	An outcrop on the Denniston Plateau on the road to the abandoned Escarpment Mine. Berlins Porphyry is mingled with Greenland Group basement rock.
Core 1	Buller Coal core samples. Core 1A at 72.50-74m depth is abundant in Greenland Group xenoliths and secondary pyrite, Core 1B at 59.60-62.30m was grey porphyry with no xenoliths, and Core 1C at 41.70-44m depth also contained many Greenland Group xenoliths.
Core 2	Solid Energy core sample at an unknown depth. Pink-grey porphyry abundant in calcite and quartz.

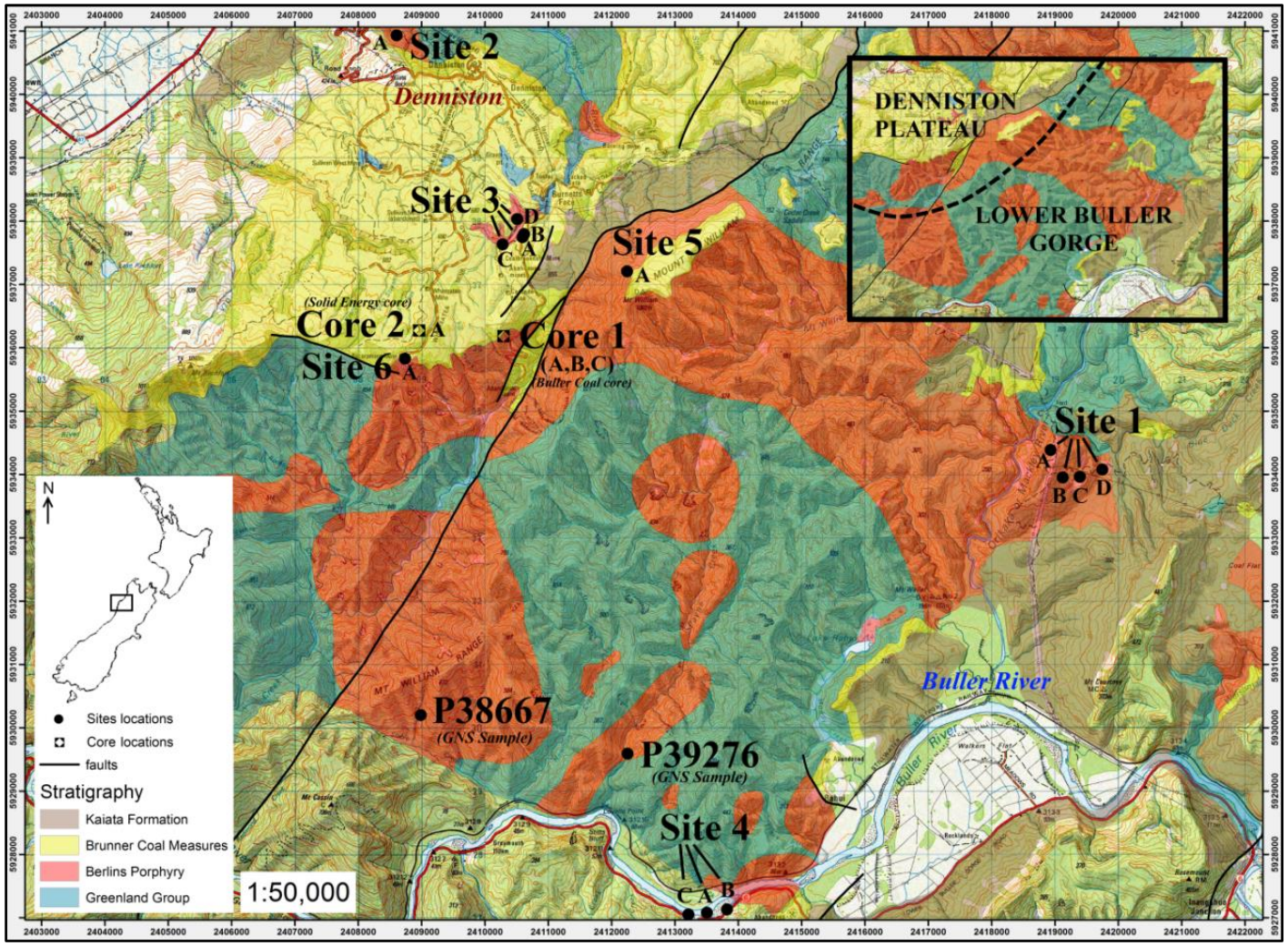

Figure 3.1: A geological map (Nathan et al. 2002) of the Berlins Porphyry (orange) that show all the sampling locations. Samples P38667 and P39276 are the GNS thin section samples that were previously sampled by Simon Nathan. Core 1 (A-C) are sourced from Buller Coal and Core 2 (A) is sourced from Solid Energy.

3.2 Mineralogical and Geochemical Analyses

Thirty one samples (Table 3.2) were cut into standard 30µm thin sections, polished, and left uncovered for mineralogical and geochemical analyses. Two covered GNS thin sections (P38667 & P39276) were added to these analyses. The mineralogy and general textures of all samples were examined with the Leica DM2500P petrographic microscope at 10x magnifications. Petrographic images were captured using the DFC 295 Camera. Samples S3B3 and S3B4 were selected for higher magnification (65x) investigations of structures within primary quartz phenocrysts. These sections were polished down to ultra-thin (20µm) sections to allow for high resolution imaging. Additionally, the quartz phenocrysts of thin section S3B4 were analysed under cathodoluminescence on the University of Canterbury's Leica 440 Scanning Electron Microscope.

Select minerals within the fine-grained porphyry samples were unidentifiable through optical microscopy and so thin sections S3A1, S3B7 and S3B11 were investigated for their mineralogy by means of wavelength dispersive X-ray spectroscopy (WDS) at the University of Otago's JEOL JXA 8600. A Smithsonian standard, Hbl 143965 (Kakanui hornblende) was used to calibrate the signals and a beam current of 20nA was applied. Spot sizes varied from 10-50µm diameters based on the minerals analysed, but the majority of the samples were analysed with 20µm diameter points. Thin section S3B2 was also investigated for its mineralogy using the University of Otago's Zeiss Sigma FEG-SEM with an Oxford instrument XMax 20 silicon drift EDS detector. Data was collected at high vacuum modes with 35Pa nitrogen pressure in the chamber.

Further mineralogical investigations included X-ray diffraction (XRD) at University of Canterbury. Sample S3B13 was ground up, ethanol was added, and then transferred to a half microscope slide and dried at room temperature. For swelling/expanding clays, the samples were placed in a desiccator with ethylene glycol solution and dried in an oven at 60°C overnight. Clay minerals affected by heat were placed into a muffle furnace for an hour at 550°C and cooled. All samples were scanned at 3 to 30°2θ .

Additionally to the mineralogical investigations twelve homogeneous Berlins Porphyry samples (10g); were analysed for their bulk geochemistry (Table 3.2). This excluded weathered porphyry

samples as their geochemical signatures were contaminated. Two altered samples from the DP (Sites 3A & B) were included in the analysis to investigate the source of the localized alteration. A complete characterization provided by ALS Minerals, Vancouver, was selected as the whole rock analysis. This package included quantifying major elements using ICP-AES and carbon and sulphur by combustion furnace. Trace elements were reported from three digestions: a lithium borate fusion for resistive elements, a four acid digestion for base metals and an aqua regia digestion for volatile gold related trace elements. The results from the whole rock analysis were displayed through Spider and Harker diagrams. The Spider diagrams plotted using IgPet (Carr, 2002) examine rare earth elements (REE) against either a standard chondrite, an ocean island basalt (OIB), a mid-oceanic ridge basalt (MORB), an E-type mid-oceanic ridge basalt (E-MORB), or a N-type mid-oceanic ridge basalt (N-MORB). Harker diagrams of SiO_2 or Fe_2O_3 against major or trace elements were plotted using Microsoft Excel. Selected trace metals were also displayed across the twelve porphyry samples to highlight variations.

3.3 Carbon Isotope Chemistry

Carbon isotopic signatures of the Berlins Porphyry were examined to identify variations between the porphyry deposits. Samples S3B12B, S3B12C, S3B13B and S3B13D were drilled with a 1mm diamond tip Dremel drill along a ten-point-transect of each sample. Pulverized rock samples ranging from 40-100mg were collected at each point. Modern organic carbon contamination i.e. skin, hair etc. was avoided by using gloves and pre-drilling every point down ~1mm before collecting samples. Sample S3B13B was drilled multiple times and treated with 50% H_2O_2 to remove organics and 4N of acetic acid (~25%) to remove carbonates. Core 1A and 1B were also analysed but only three samples per core were collected. Each core was crushed and pulverized into a powder using a ring mill.

All samples were analysed for their carbon weight percentage and $\delta^{13}C‰$ values using the University of Canterbury's Costech Elemental Combustion System (ECS) 4010 and the Thermofinningan Delta V+ Gas Isotope Ratio Mass Spectrometer (GIRMS). Conflow III was used to control gas flow between the ECS and GIRMS. The $\delta^{13}C$ values were determined (of CO_2) by combusting samples at 1080°C, under continuous flow of ultra-high purity (99.9999%) helium. An empty autosampler well was left between every sample during analysis to ensure the signal of each

sample was not contaminated by residual combustible material of adjacent samples. Percentage of carbon by mass and volume were determined by measuring the yield of precisely massed (±1 mg) certified reference materials of known carbon content.

Table 3.2: A rock catalogue of Berlins Porphyry samples and their corresponding analysis

Sample	Type of Sample	Easting	Northing	Analysis
S1A1	Type E – Weathered Hyalodacite	2418968	5934391	P/WR
S1A2	Type A - Hyalodacite	2418968	5934391	P
S1B1	Type C - Granodiorite	2419085	5933996	WR
S1B2	Type C– Slightly Weathered Granodiorite	2419085	5933996	P
S1C1	Type A - Hyalodacite	2419325	5934011	P
S1C2	Granodiorite Spheroidal Structure	2419325	5934011	P
S1D1	Type A - Hyalodacite	2419661	5934128	WR
S1D2	Type A - Hyalodacite	2419661	5934128	P
S1D3	Hyalodacite Spheroidal Structure	2419661	5934128	P
S2A1	NA - Weathered Porphyry	2408725	5940959	-
S3A1	Type G – Hydrothermally Altered Hyalodacite	2410927	5938016	P/EM
S3A2	Type G - Hydrothermally Altered Hyalodacite	2410927	5938016	WR
S3B1	Type G - Hydrothermally Altered Hyalodacite	2410944	5938032	P/WR
S3B2	Fe-rich Boulder-like Structure	2410944	5938032	P/EDS
S3B3	Fe-rich Boulder-like Structure	2410944	5938032	P
S3B4	Rim of Fe-rich Boulder-like Structure	2410944	5938032	P/CL
S3B5	NA – Weathered Fe-rich Boulder-like Structure	2410944	5938032	-
S3B6	Fe-rich Boulder-like Structure	2410944	5938032	P
S3B7	Cross-section – Fe-rich Boulder-like Structure	2410944	5938032	P/EM
S3B8	Cross-section – Fe-rich Boulder-like Structure	2410944	5938032	P
S3B9	Fe-rich Boulder-like Structure	2410944	5938032	P
S3B10	Fe-rich Boulder-like Structure	2410944	5938032	P
S3B11	Type G - Hydrothermally Altered Hyalodacite	2410944	5938032	P/EM
S3B12	Fe-rich Boulder-like Structure	2410944	5938032	P/C
S3B13	Fe-rich Boulder-like Structure	2410944	5938032	P/C/XRD
S3C1	Type A – Hyalodacite	2410379	5937710	WR
S3C2	Type A - Hyalodacite	2410379	5937710	P
S3D1	Type A - Hyalodacite	2410520	5937909	P/WR
S4A1	NA - Brunner Coal Measures	2413695	5926971	-
S4B1	Type B - Hyalodacite	2413787	5927054	P/WR
S4B2	Type F – Microgranodiorite	2413787	5927054	P
S4C1	Type E – Weathered Hyalodacite	2413449	5927012	P
S5A1	Type A - Hyalodacite	2412192	5937220	P/WR
S6A1	Type D – Fluid-Altered Granodiorite	2408905	5935948	P
S6A2	NA – Weathered Porphyry	2408905	5935948	-
S6A3	Type D – Fluid-Altered Granodiorite	2408905	5935948	WR
Core 1A	Type A - Hyalodacite	2410365	5936156	P/C
Core 1B	Type C - Granodiorite	2410365	5936156	P/WR/C
Core 1C	Type A - Hyalodacite	2410365	5936156	P/WR
Core 2A	Type A - Hyalodacite	2409023	5936687	P
P38667	Type C– Granodiorite (Thin Section Only)	2408989	5933023	P
P39276	Type A– Hyalodacite (Thin Section Only)	2412315	5929678	P

GG = Greenland Group; P = Petrographic Analysis; WR = Whole Rock Analysis; C = Carbon Isotope Analysis; XRD = X-ray Diffraction; EM = Electron Microprobe; EDS = Scanning Electron Microscopy; CL = Cathodoluminescence. Co-ordinates in New Zealand Transverse Mercator Projection.

Chapter Four – Results

4.1 Field Sampling

Sampling the Berlins Porphyry shows LBG samples are extremely weathered and DP samples are hydrothermally altered. Figure 4.1 shows images of the six sampling sites and the variation across the LBG and DP.

Lower Buller Gorge Samples

The LBG is a large area covered in extensive vegetation and waterways producing highly weathered samples. The porphyry samples in the LBG vary from pink to grey in colour and fine-grained to coarse-grained in texture. Site 4 (Fig. 4.1) hosts a large microgranodiorite outcrop and two small hyalodacite outcrops. Site 1 (Fig. 4.1) identifies weathered hyalodacite adjacent to granodiorite, but no boundary is evident. Additionally, Site 1D contains boulder-like structures encased in porphyry (Fig. 4.2 A), which in cross-section display two mineralization layers: a weathered clay and hematite-rich rim and an unaltered porphyry centre (Fig. 4.2 B).

Denniston Plateau Samples

The DP outcrops are dispersed over a smaller area and are recently exposed through the mining of the unconformably overlying Brunner Coal Measures. Outcrops on the DP display a large mineralogical and textural variation between sites. For example, Site 3 hosts an unaltered porphyritic hyalodacite and a white iron stained, and a highly altered porphyritic dacite with embedded Fe-rich boulders (Fig. 4.1). Cross-sections of the boulders indicate three mineralization layers (Fig. 4.3): an outer hematite rim, an inner magnetite layer and a white altered porphyry centre. The concentrated precipitation of magnetite around other mineralogy (Fig. 4.3) highlights these structures are concretions (Chan et al. 2005). Site 5 (Fig. 4.1) hosts a dark green unaltered porphyritic hyalodacite and Site 6 (Fig. 4.1) displays a coarse-grained granodiorite mingled with basement Greenland Group.

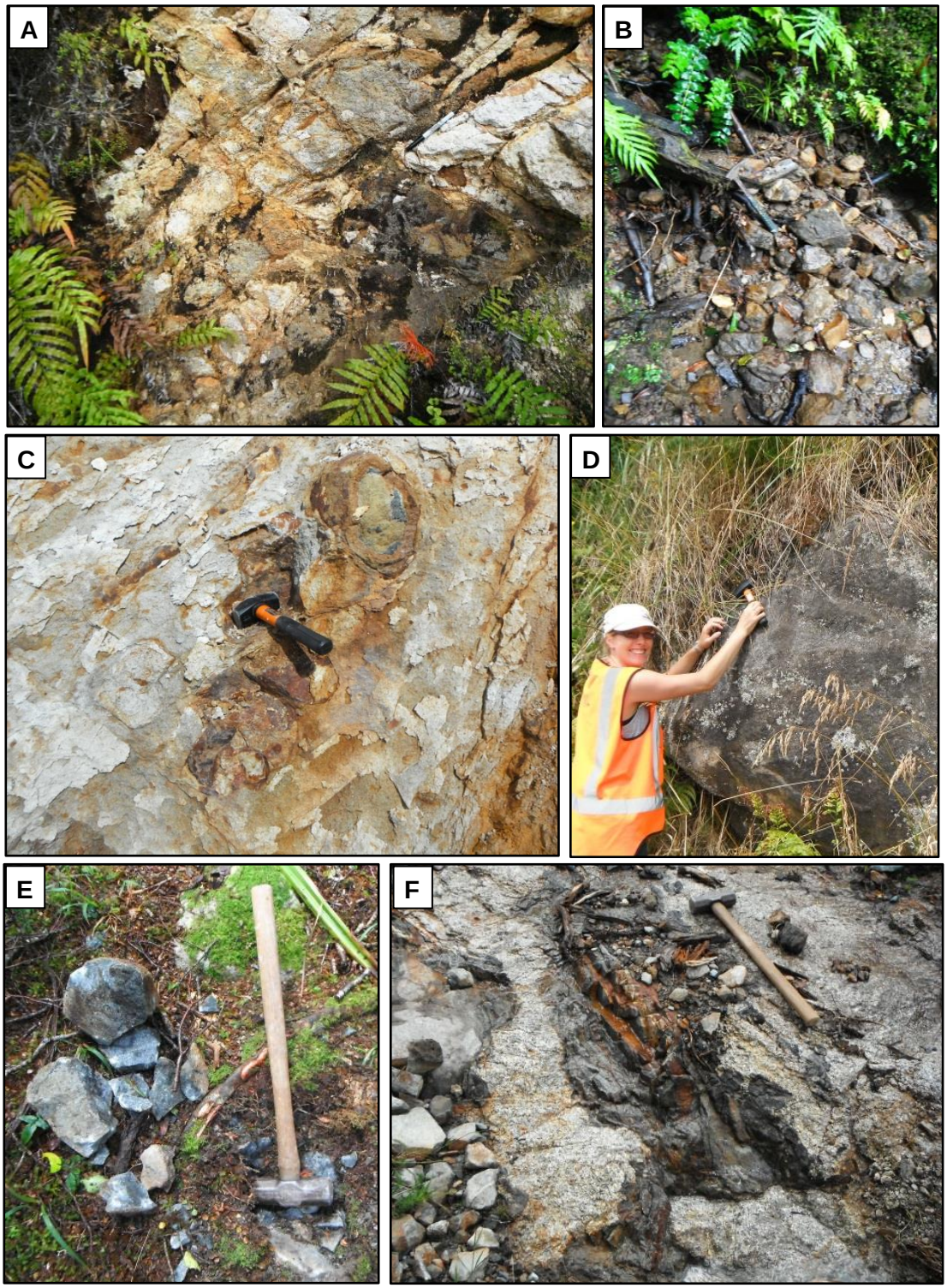

Figure 4.1: Field photographs of all the Berlins Porphyry sampling sites. Image (A) displays Site 1D with boulder-like structures encased in weathered porphyry. Image (B) shows outcrop Site 2A at Conns Creek. Image (C) is Site 3B, a highly altered white and iron stained porphyry with embedded Fe-rich concretions. Image (D) is Site 4A, a grey hyalodacite and image (E) is Site 5A, a dark green hyalodacite. Image (F) shows Site 6A, which represents a mingled contact between the coarse-grained granodiorite and the basement Greenland Group.

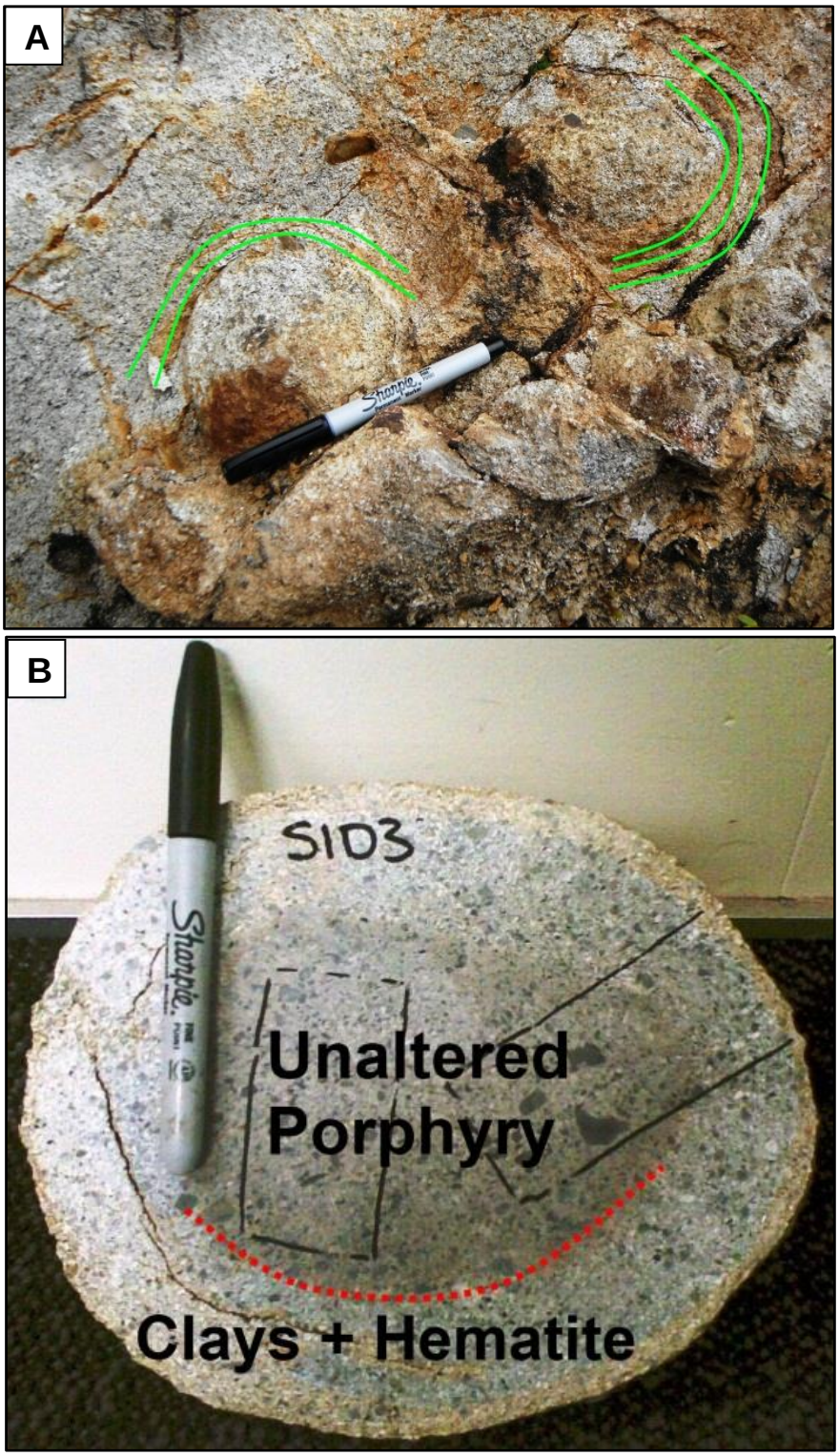

Figure 4.2: Two photographs of the boulder-like structures in the LBG at Site 1D. Image (A) displays the boulders wrapped in layers of clay and hematite (green). Image (B) shows a cross-section of one of the boulders (S1D3) that highlights the weathered rim and unaltered core of the structure.

Figure 4.3: An image showing the cross-section of a Fe-rich concretion from Site 3B on the Denniston Plateau. Three layers are shown; an outer hematite rim, an inner magnetite layer and a white altered porphyry centre.

4.2 Petrographic Analysis

Mineralogy and textural observations of thirty three thin sections are used to categorise the Berlins Porphyry into seven types; (A) to (G). These categories are briefly outlined below and discussed in detail in Table 4.1. All samples host primary resorbed quartz phenocrysts. For full mineralogical and textural observations of each thin section refer to the Appendix.

Type A porphyry (Fig. 4.4 A) is a porphyritic hyalodacite containing fragmented phenocrysts of plagioclase feldspar, biotite and resorbed quartz within a glassy and fragmented crystalline groundmass. The glassy groundmass displays marginal foliations (Fig. 4.5 A) and typically primary plagioclase phenocrysts are replaced with either sericite (Fig. 4.5 B) or calcite. Accessory mineralogy includes alkali feldspar and igneous magnetite (often replaced by pyrite).

Type B porphyry (Fig. 4.4 B) is also a hyalodacite, but shattered phenocrysts of quartz and plagioclase remain in their primary crystal shapes and the groundmass comprises <20% of the entire rock.

Type C porphyry (Fig. 4.4 C) is a phaneritic granodiorite with large euhedral interlocking crystals of quartz, plagioclase, alkali feldspar and biotite. The feldspars are replaced by sericite or calcite (Fig. 4.6 A) and other accessory minerals include muscovite, chlorite and calcitic veins (Fig. 4.6 B).

Type D porphyry (Fig. 4.4 D) hosts micro-deformed biotite and recrystallized quartz veins within a marginally foliated, biotite-rich, coarse-grained rock. Recrystallized xenoliths of Greenland Group are prevalent and contain fine-grained quartz, biotite and clay mineralogy.

Type E porphyry (Fig. 4.4 E) is a weathered hyalodacite containing primary resorbed quartz phenocrysts, clays and hematite. All other mineralogy has been replaced.

Type F porphyry (Fig. 4.4 F) is a microgranodiorite with sub-hedral, medium-grained, interlocking and partially fractured quartz, plagioclase feldspar, alkali feldspar and biotite crystals.

Type G porphyry (Fig. 4.4 G) is a white altered porphyry with primary resorbed quartz phenocrysts, muscovite, magnetite, recrystallized quartz and clays. Relics of primary biotite phenocrysts are visible, but replaced by iron oxides and clays.

Table 4.1: The types of porphyry identified within the Berlins Porphyry

Type	Name	Minerals Present & Average %	General Textures
A	Hyalodacite	Primary: quartz (20%), plag (15%), biotite (8%), k-spar (1-3%) Accessory: Greenland Group xenoliths (4%), calcite (2%) pyrite, muscovite (1%), magnetite (1%)	Porphyritic. Groundmass predominantly volcanic glass and broken phenocrysts. Phenocrysts are resorbed and broken. Calcite replaces feldspars, some micro-deformation of biotite.
B	Hyalodacite	Primary: quartz (25%), plag (15%), k-spar (10%), biotite (3%) Accessory: hematite (10%), muscovite (2%)	Porphyritic. Shattered phenocrysts retaining original shape, interstitial hematite, small groundmass.
C	Granodiorite	Primary: quartz (30%), plag (25%), k-spar (10%), biotite (10%) Accessory: chlorite (1-5%), hematite (<5%), pyrite, (4%), muscovite (8%), calcite (1-5%)	Phaneritic. Euhedral interlocking crystals, mineral inclusions, resorbed larger phenocrysts, secondary calcite veins, calcite/sericite replaces feldspars.
D	Fluid-Altered Granodiorite	Primary: biotite (40%), quartz (20%) Accessory: opaques (10%), calcite (<5%), muscovite (<5%), GG xenoliths (30%)	Phaneritic. Secondary biotite and recrystallized quartz veins, micro-deformation of biotite, large Greenland Group xenoliths, foliation.
E	Weathered Hyalodacite	Primary: quartz (20%), biotite (<5%) Accessory: clays (25%), hematite (20%), muscovite (1%)	Porphyritic. Hematite replaces biotite and clays replace feldspar phenocrysts. Resorbed quartz remains.
F	Microgranodiorite	Primary: quartz (35%), plag (15%), k-spar (10%), biotite (5%) Accessory: muscovite (5%), hematite (5%), calcite (5%), magnetite (5%)	Medium interlocking sub-hedral crystals, groundmass is broken crystals and recrystallized quartz, biotite replaced by hematite.
G	Hydrothermally Altered Hyalodacite	Primary: clays/white micas (70%), quartz (20%) Accessory: hematite (5-10%), magnetite (<5%)	Altered porphyritic dacite (type A). Primary resorbed quartz remains, but the remaining mineralogy is secondary hydrothermal mineralization.

Rounded Features	Minerals Present	General Textures
Denniston Plateau	Quartz (10-30%), hematite (20-40%), magnetite (15-30%), clays/white micas (15-35%)	Two-three layers; hematite, magnetite and an altered porphyry core (type G). Primary and recrystallized quartz within all three layers. Secondary hydrothermal clays and micas (petrographically unidentifiable).
Lower Buller Gorge	Quartz (20-25%), biotite (5%), chlorite (10%), alkali feldspar (3%), plagioclase feldspar (8%), hematite (20%), magnetite (5%), clay minerals (10-20%)	Porphyritic. Biotite alters to magnetite and chlorite. Outer edge abundant in hematite and clays. Centre is predominantly type A and C porphyry with additional chlorite and magnetite.

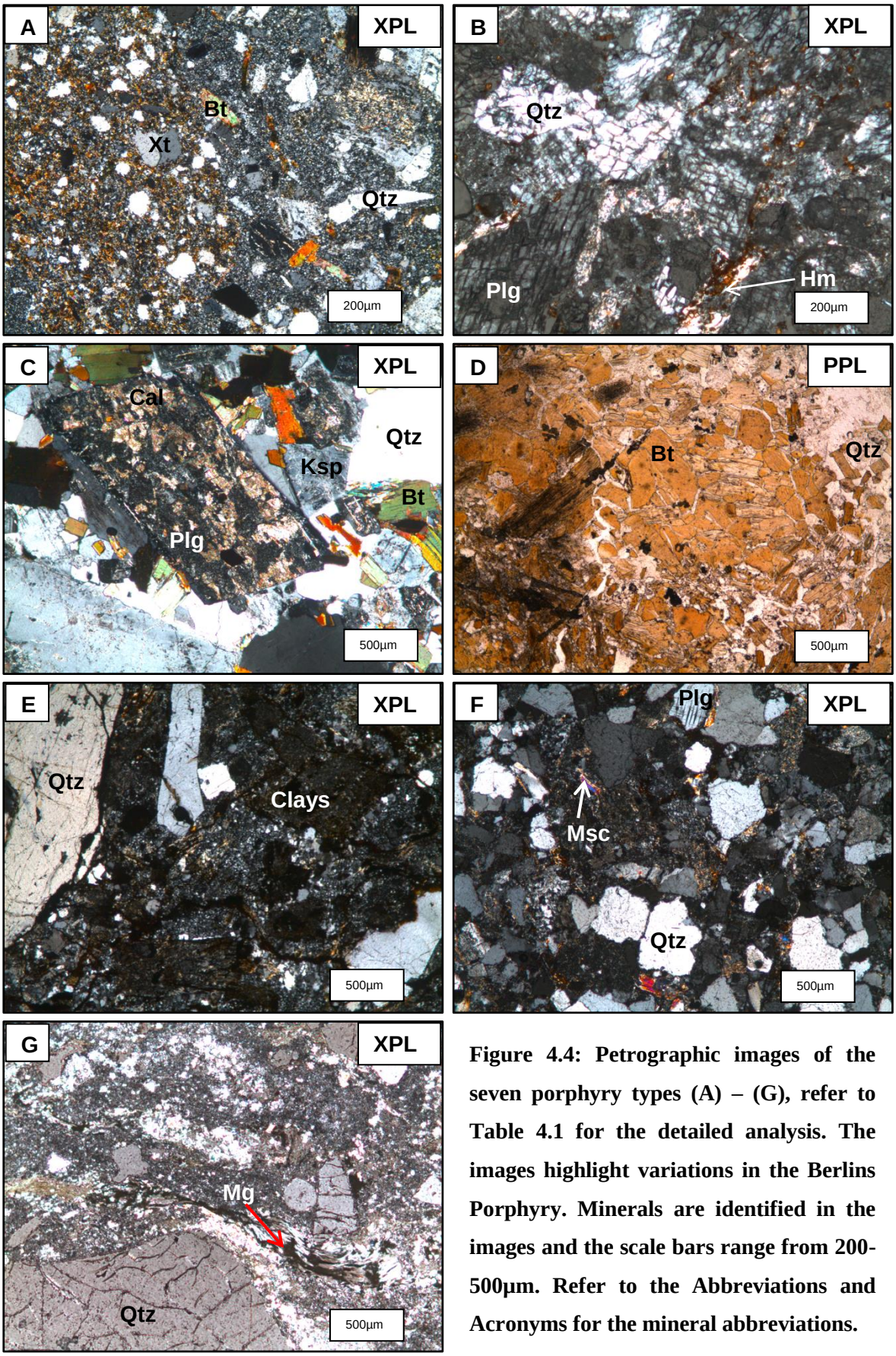

Figure 4.4: Petrographic images of the seven porphyry types (A) – (G), refer to Table 4.1 for the detailed analysis. The images highlight variations in the Berlins Porphyry. Minerals are identified in the images and the scale bars range from 200-500µm. Refer to the Abbreviations and Acronyms for the mineral abbreviations.

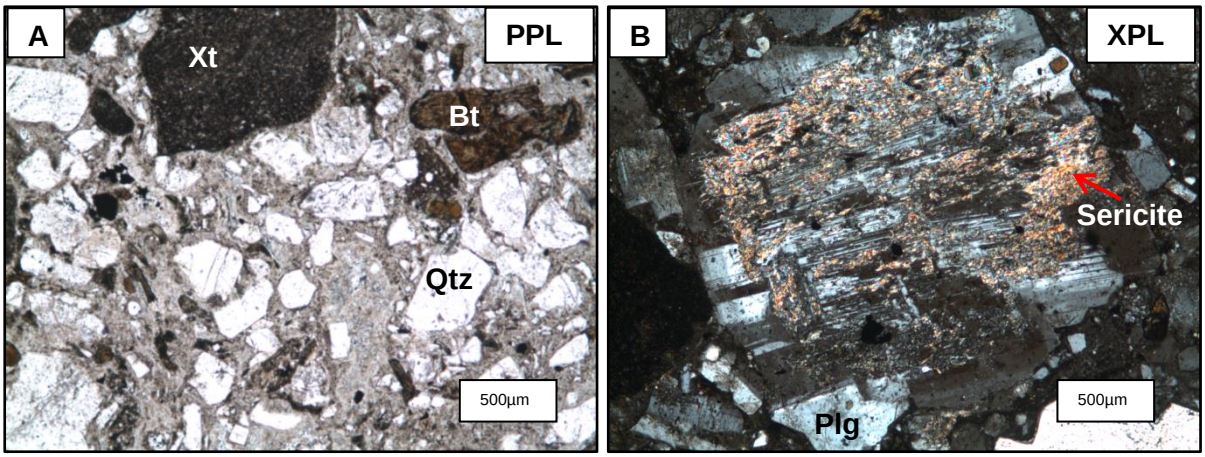

Figure 4.5: Two petrographic images of Type A porphyry. Image (A) shows marginal foliations in a glassy groundmass and image (B) displays sericitic alteration of a plagioclase feldspar phenocryst.

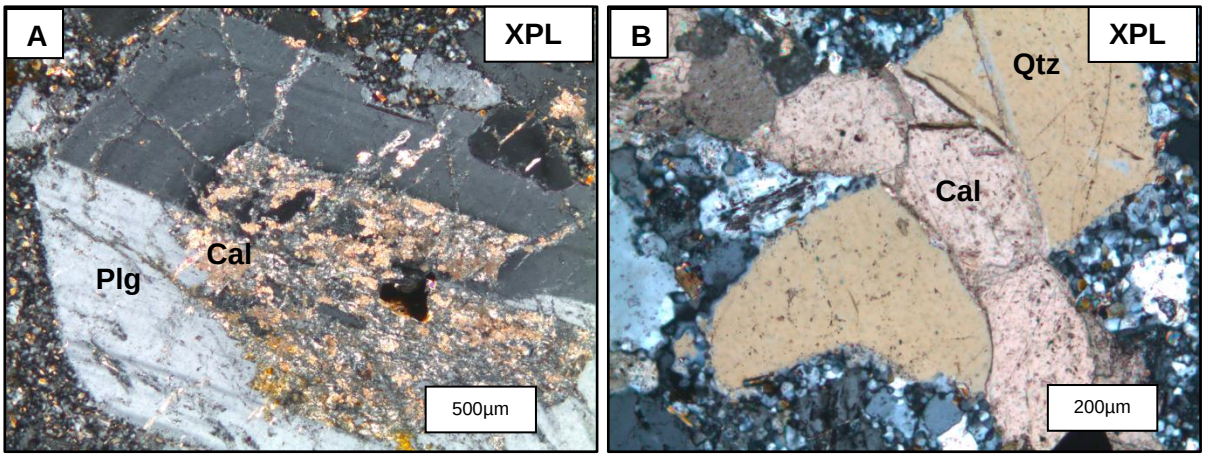

Figure 4.6: Two petrographic images that display the forms of secondary calcite within the Type C porphyry. Image (A) displays a zoned igneous calc-plagioclase feldspar being replaced by calcite and image (B) highlights the cross-cutting nature of a calcitic vein.

In addition to the seven porphyry types two structures are present within the Berlins Porphyry and show additional mineralogical and textural variations (Table 4.1). The LBG rounded structures at Site 1D show evidence of chloritization. Chlorite and magnetite replace biotite along crystal rims and cleavage planes (Fig. 4.7 A). Outer edges of the LBG structures display a weathering effect as feldspars, biotite, magnetite, and chlorite are replaced by clays and hematite (Fig. 4.7 B).

In contrast, Fe-rich concretions on the DP, specifically sites 3A and B, display three well-defined mineralization layers (Fig. 4.8 A). The altered porphyry (Type G) is located in the centre of the concretions; refer to Section 4.21 and Table 4.1 for mineralogical and textural analyses. The inner magnetite layer (Fig. 4.8 A & B) is comprised of primary resorbed quartz phenocrysts, muscovite, recrystallized quartz, magnetite and clay minerals. This layer has a gradational contact with the white altered porphyry and is compositionally similar. Magnetite crystals (Fig. 4.9) vary from broken prismatic, angular finger-like shapes (Fig. 4.9 A) to well-formed rounded cubic and hexagonal shapes often linking in chains (Fig. 4.9 C & D). Individual rounded magnetite crystals range in diameter from <1µm to 5µm and typically accumulate in large masses (Fig. 4.9 B).

Additionally, the magnetite layer hosts filamentous structures, tubular hollows and spherical hollows. The filamentous structures cross-cut hydrothermal mineralization (Fig. 4.10 A & B), are typically <300µm long and <20µm wide, and often exhibit segmentation (Fig. 4.10 B). The tubular hollows and spherical depressions (Fig. 4.10 C-E) reside within primary quartz phenocrysts and are partially or completely in-filled with rounded magnetite crystals (Fig. 4.9 C). These structures are typically 5-20µm wide and display smooth and round-edged interconnected networks (Fig. 4.10 C) that lead into variably sized spherical depressions (Fig. 4.10 E). The outer layer overprints the previous two mineralization layers and shows hematite encasing all mineralogy except the primary quartz phenocrysts (Fig. 4.8 B). Additional crystal morphologies within the hematite layer include rounded globular hematite clusters or single hematite ball-like structures (Fig. 4.10 F).

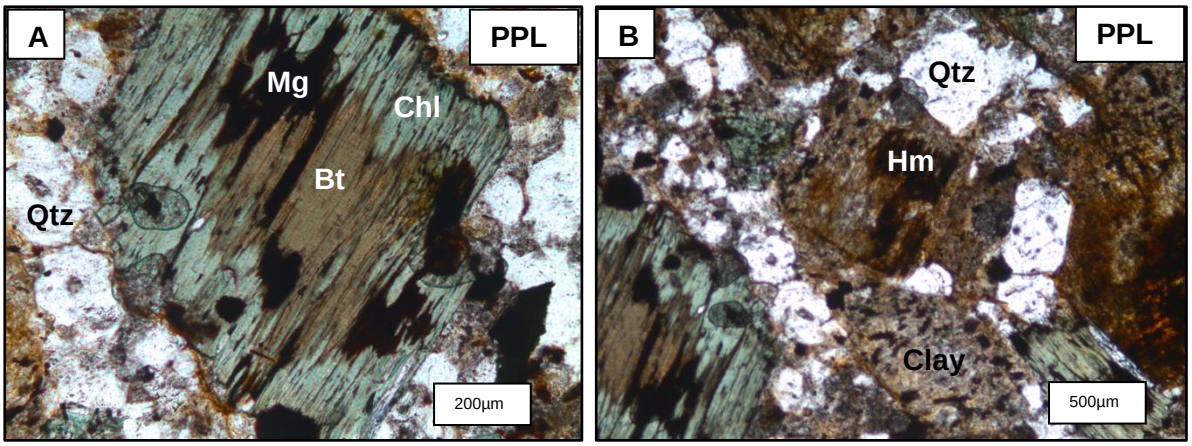

Figure 4.7: Petrographic images of the sample S1C2, a spheroidal boulder. Image (A) shows chlorite and magnetite alteration around the rim and within cleavage planes of a biotite phenocryst. Image (B) displays weathering of a spheroid, where feldspars, biotite and chlorite are replaced by clays and hematite mineralization.

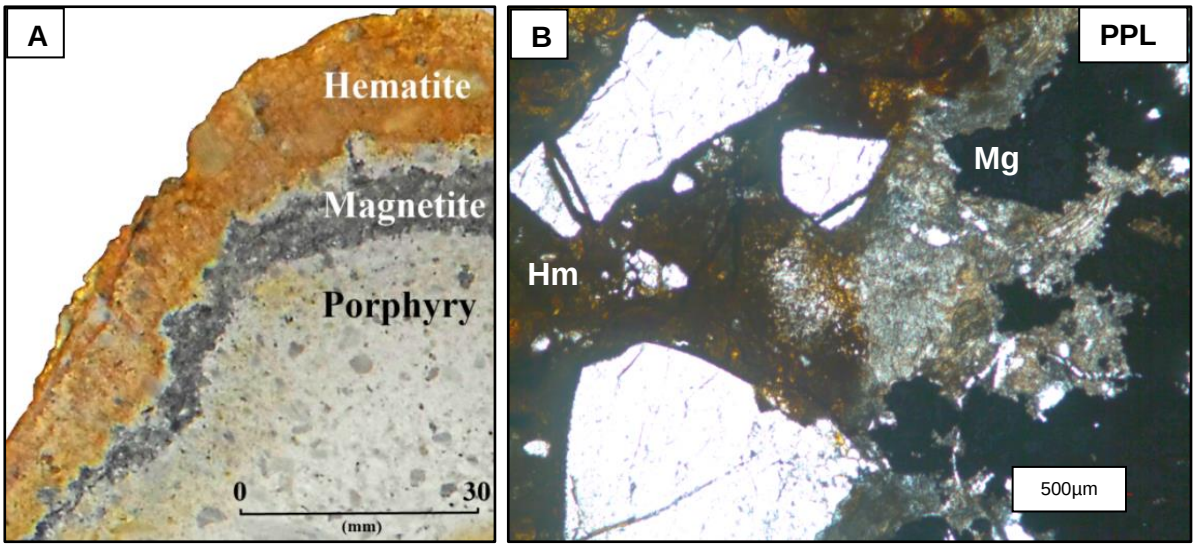

Figure 4.8: Two images that show the three mineralization layers within the iron concretions. Photograph (A) shows a cross-sectional view of the concretion and the petrographic image (B) displays the hematite and magnetite layering.

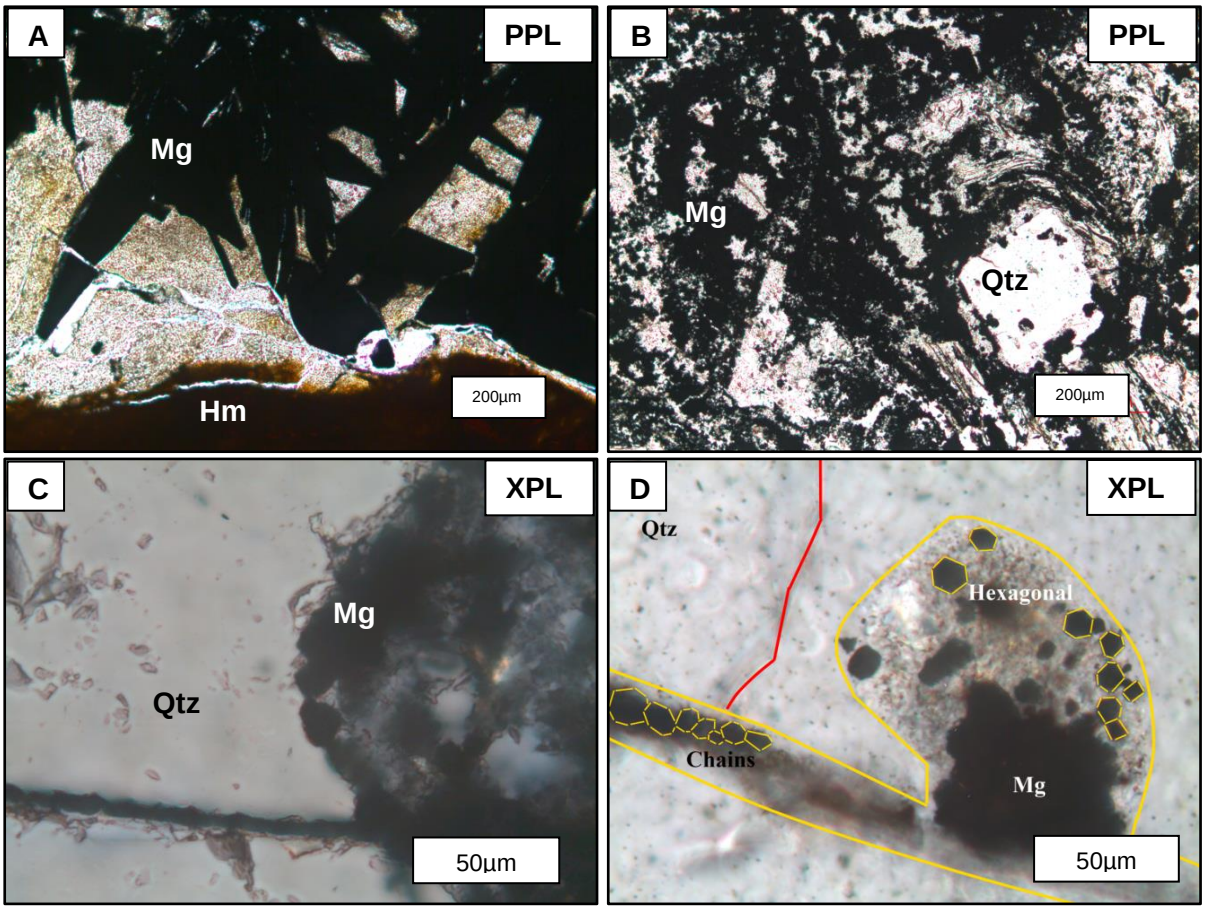

Figure 4.9: Four petrographic images of the different types of magnetite morphologies. Image (A) displays the prismatic and angular, finger-like morphologies, whilst image (B) shows rounded magnetite crystals accumulating in masses. Images (C) & (D) show the individual size of rounded cubic or hexagonal magnetite crystals and they also highlight the existence of magnetite chains. The red line in image (D) represents a cooling fracture in the quartz phenocryst, but the yellow lines highlight the presence of another more rounded structure within the quartz phenocryst.

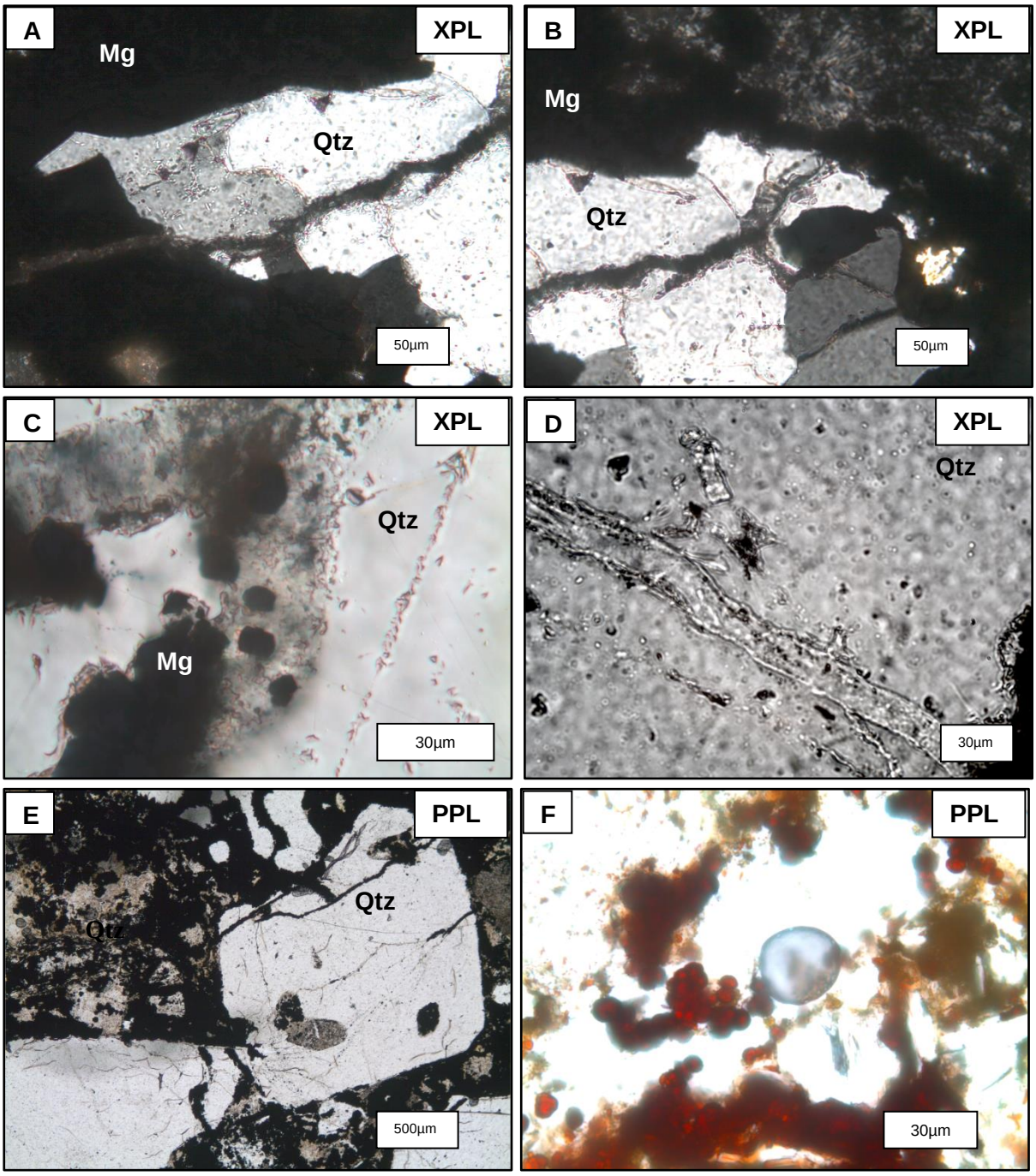

Figure 4.10: Eight petrographic images that show the structures within the Berlins Porphyry iron concretions. Images (A) & (B) show filamentous branching structures cross-cutting recrystallized quartz and additionally, image (B) displays segmentation of a filament. Images (C), (D) & (E) show tubular hollows within primary quartz phenocrysts that can be partially or completely in filled with rounded magnetite crystals. Images (C) & (D) also highlight the rounded and smooth-edged morphologies of these tubular depressions. Image (E) also highlights the branching network of tubular depressions that lead into the spherical hollows. Image (F) displays rounded globular hematite clusters that are present within the outer hematite layer of the iron concretions.

4.3 Electron Microprobe Analysis

Electron microscopy results indicate the presence of muscovite/sericite, quartz and kaolinite within samples S3A1, S3B7 and S3B11 (Table 4.2). Identifications are based on previous geochemical signatures of minerals provided by Deer et al. (2004). Imaging of these samples displays new textures within the alteration mineralogy. The presence of a coalescent texture between kaolinite and muscovite (Fig. 4.11 D) suggests these two minerals crystallized simultaneously (Winter, 2010). Pseudomorphic biotite crystals that display geochemical signatures of kaolinite highlight a complete mineral replacement (Fig. 4.11 C). Figure 4.11 shows 20µm to 50µm diameter spot locations on the minerals analysed.

4.4 Scanning Electron Microscopy - Energy Dispersive X-ray Spectroscopy

Energy dispersive spectroscopy (EDS) on sample S3B2 highlights a sulphur peak within the magnetite crystals (Fig. 4.12 A), which indicates pyritization. Additionally, segments of recrystallized quartz show aluminium (Al) and potassium (K) peaks (Fig. 4.12 B) highlighting the presence of an alkali feldspar that is interlocked with recrystallized quartz. A carbon signal is also shown in this sample, but due to poor sample preparation the origin of the carbon could be either from an ancient microbial source or a modern organic contamination.

4.5 Cathodoluminescence

Cathodoluminescence of sample S3B4 shows the tubular structures within the primary quartz phenocrysts are fed by micro-cracks (Fig. 4.13 D & F) and petrographic analysis identifies rounded magnetite crystals within the tubular structures (Fig. 4.13 A & B). Quartz containing no titanium (no luminescence – black) in fills tubular structures within the primary quartz phenocrysts (Fig. 4.13 D & F). These structures were unidentifiable through petrographic and scanning electron imaging (SEI); (Fig. 4.13 A, B, C, F).

4.6 X-ray Diffraction

X-ray diffraction results show that sample S3B13 hosts quartz, muscovite, kaolinite and sanadine. The database matches crystalline components represented on the XRD trace charts (Fig. 4.14); refer to the Appendix for all the trace charts. Quartz peaks heavily overprint muscovite, kaolinite and sanadine (Fig. 4.14).

Table 4.2: Electron microprobe signatures of minerals from the altered porphyry

Oxides	**Muscovite**					**Kaolinite**				**Quartz**
(wt %)	**S3B7**	**S3B7**	**S3B11**	**S3B11**	**S3A1**	**S3B7**	**S3B7**	**S3B11**	**S3B11**	**S3A1**
Na_2O	0.31	0.23	0.38	0.42	0.3	0.06	0.08	0.06	0.06	0
K_2O	11.07	11.16	10.38	10.6	10.68	0.14	0.41	0.07	0.19	0.02
SiO_2	44.76	46.06	44.93	43.78	44.39	44.63	40.41	45.58	46.34	99.24
TiO_2	0.05	0.56	0.52	0.49	0.41	0.02	0.07	0.33	0.65	0.06
Al_2O_3	36.1	31.27	32.49	32.01	32.06	40.33	35.88	40.65	40.39	0.45
MnO	0.04	0.1	0.11	0.08	0.1	0.01	0.04	0.04	0.05	0.03
MgO	0.57	1.91	1.98	2.3	2	0.12	0.08	0.04	0.1	0.05
CaO	0	0	0	0	0	0.03	0.08	0.03	0.07	0
FeO	2.29	4.73	4.09	4.58	4.35	0.53	1.86	0.04	0.26	0.06
Total	**95.19**	**96.02**	**94.88**	**94.26**	**94.29**	**85.87**	**78.91**	**86.84**	**88.11**	**99.91**

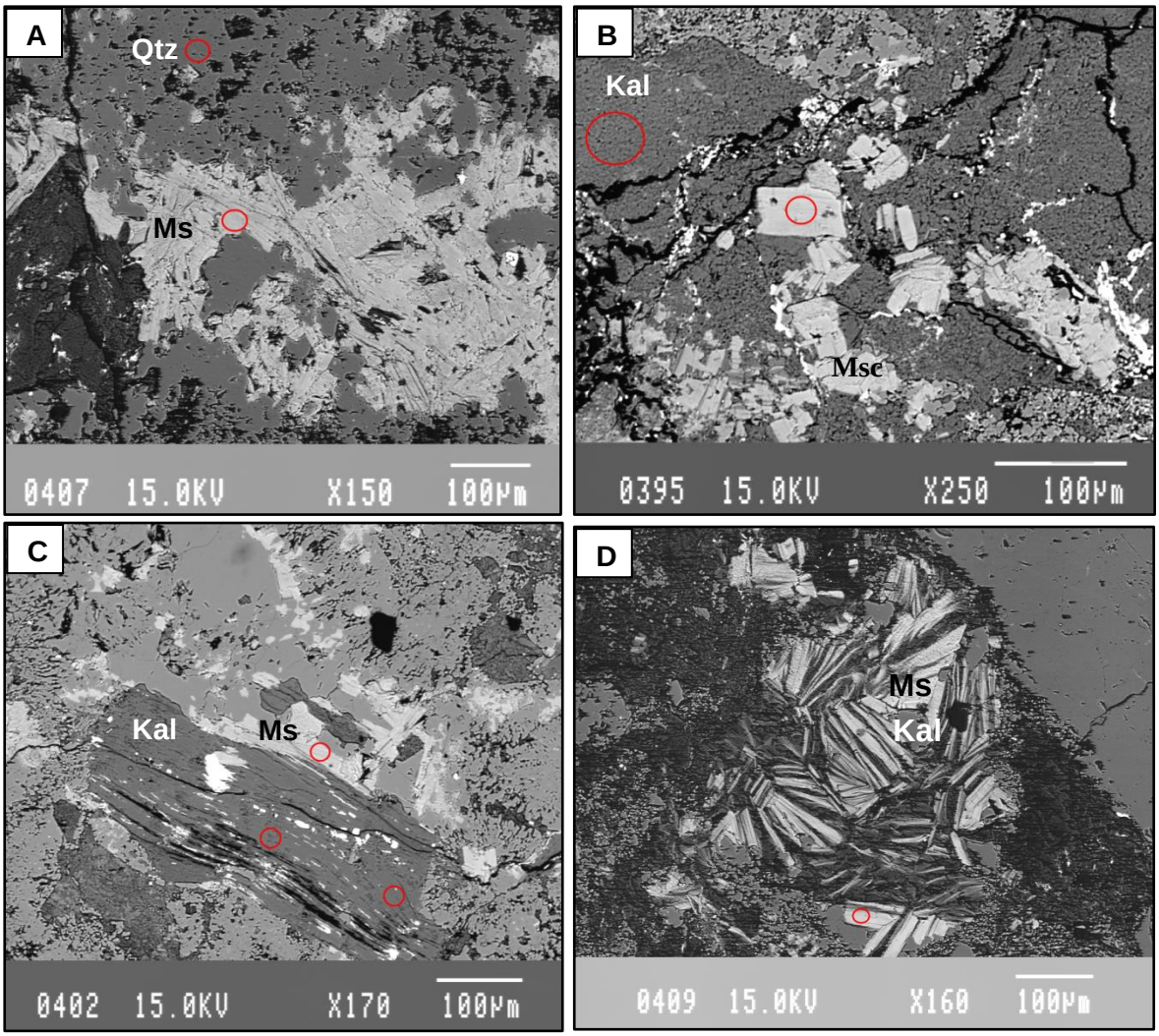

Figure 4.11: Backscatter images from the electron microprobe analysis of samples S3A1, S3B7 and S3B11. Image (A) shows sample S3A1 hosting recrystallized quartz and muscovite, image (B) displays sample S3B7 containing kaolinite and muscovite and image (C) shows sample S3B11 with muscovite and kaolinite replacing biotite phenocrysts. Image (D) shows the coalescence texture between muscovite and kaolinite in sample S3B11 of the white altered porphyry.

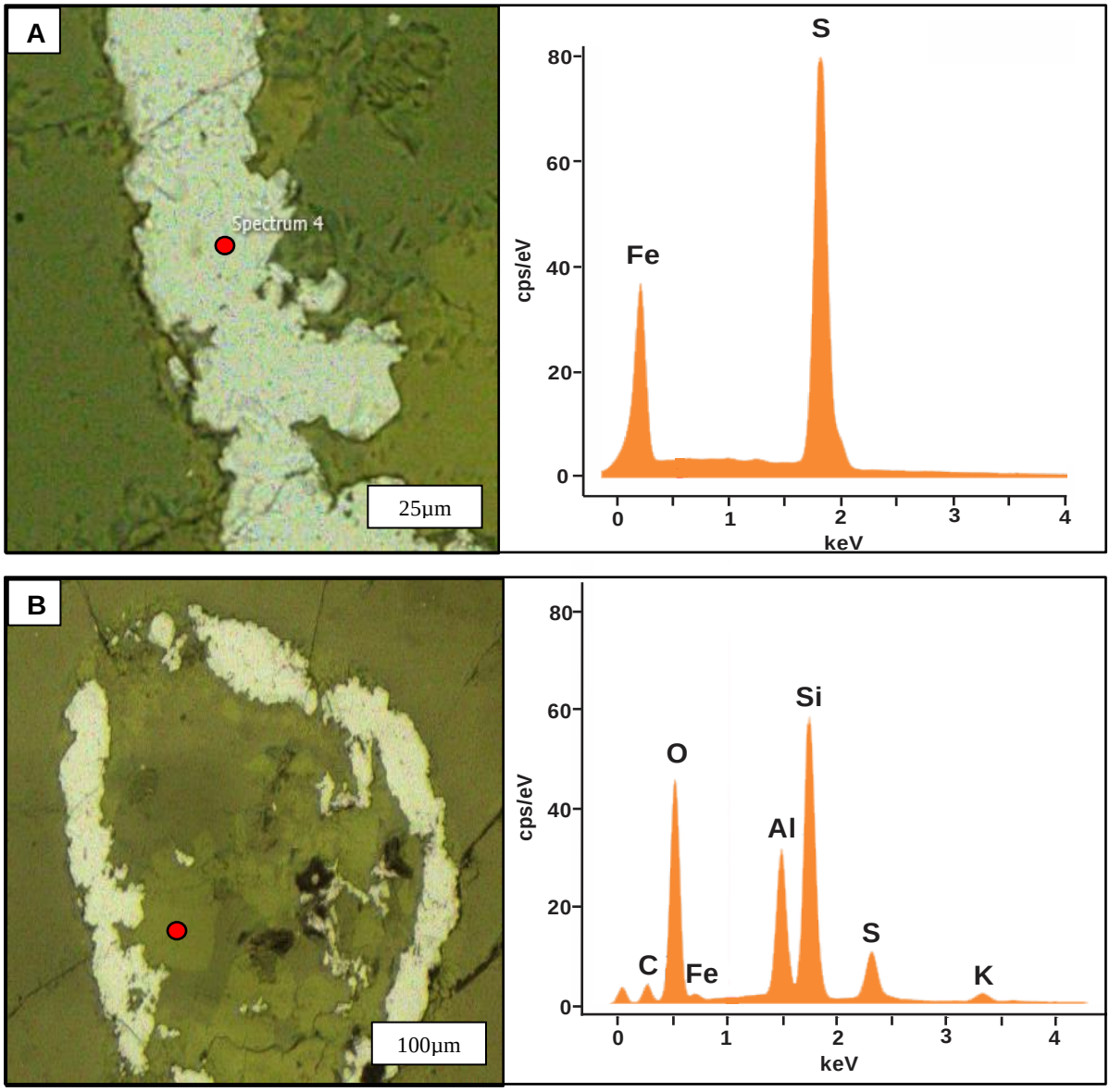

Figure 4.12: Two images from SEM-EDS analysis, where the red dots are the analysed spot locations. The white mineral displays a sulphur peak in spectra (A) and the lighter green/grey mineral shows potassium and aluminium peaks in spectra (B). No elemental percentages were calculated during the analysis, but the spectrum indicates relative percentages. Spectra (B) also show sulphur, iron and carbon peaks alongside the aluminium, silica, oxygen and potassium. These are interference signals from the adjacent white minerals.

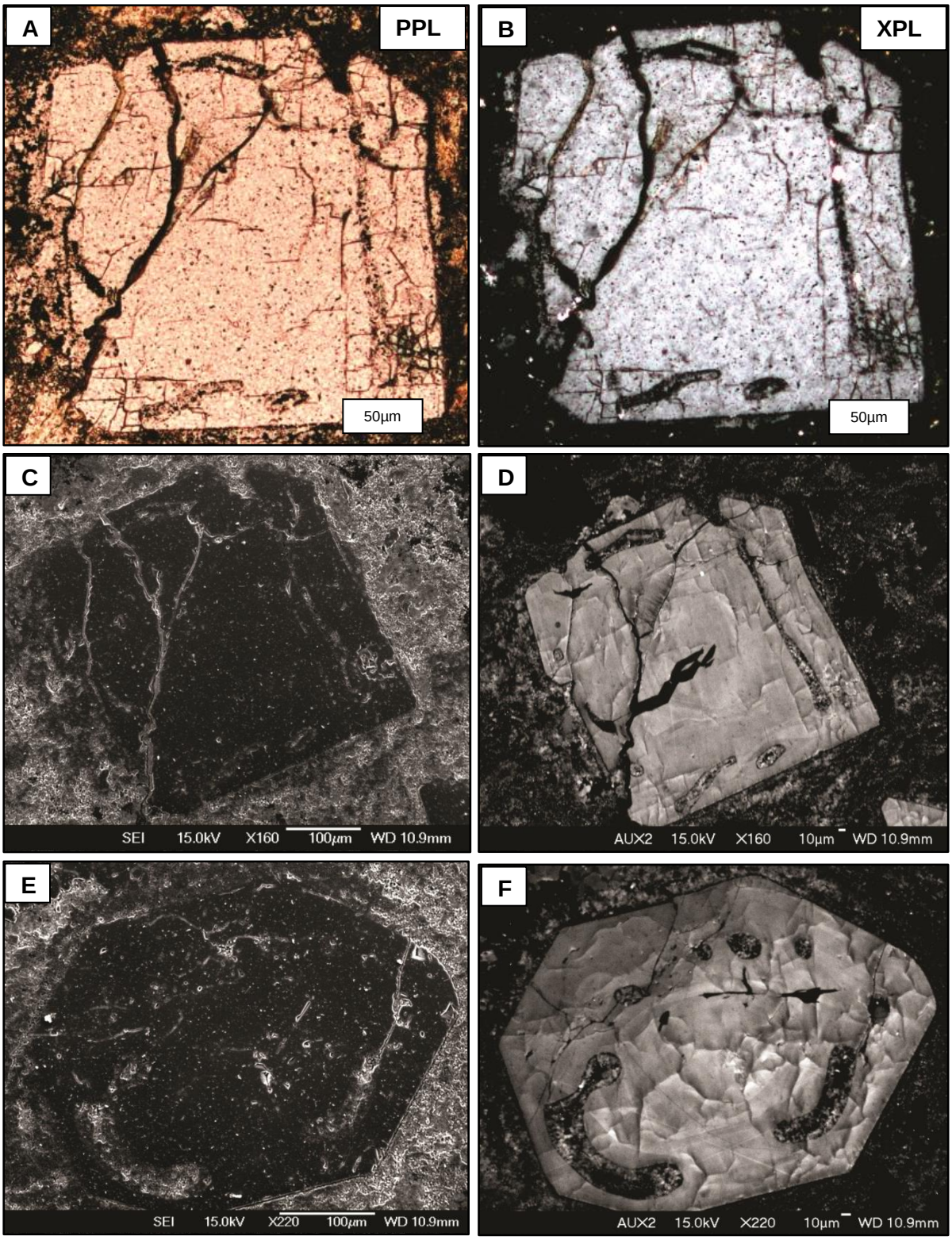

Figure 4.13: Petrographic, scanning electron microscopy, and cathodoluminescence images of two primary quartz crystals from sample S3B4. Petrographic images (A) & (B) are in plane (PPL) and crossed polarized light. They show rounded iron oxides in filling tubular structures. Images (C) & (E) are secondary electron images and images (D) & (F) are cathodoluminescence images highlighting the tubular structures and black titanium-deficient quartz.

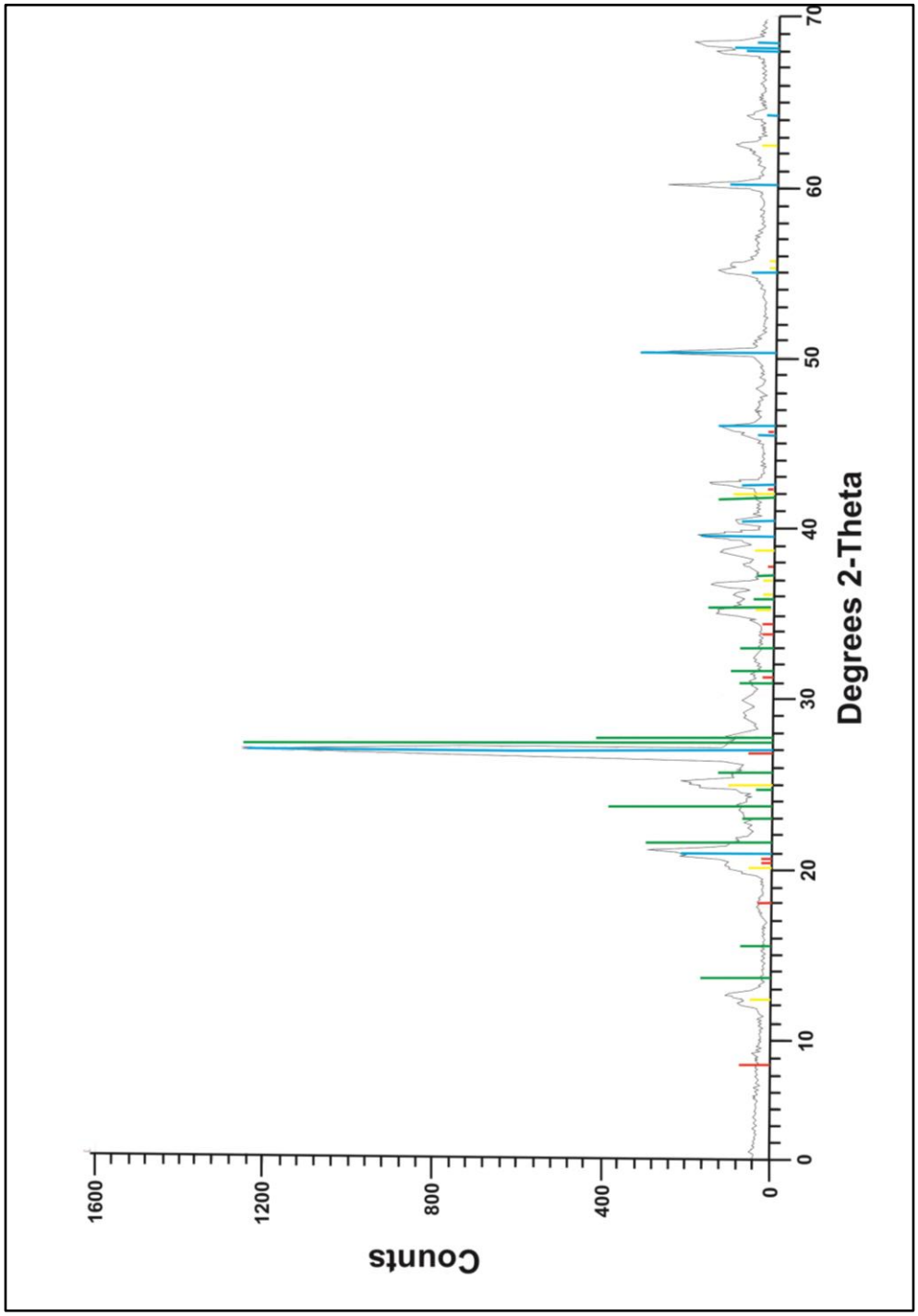

Figure 4.14: An example of the scanned XRD trace charts. Blue is quartz, green is sanadine, yellow is muscovite/sericite and red is kaolinite. The large peaks are the quartz signals.

4.7 Whole Rock Analysis

Whole rock analysis of the Berlins Porphyry indicates geochemical variations between the twelve analysed porphyry samples as shown in Figures 4.15 & 4.16. Harker diagrams of SiO_2 plotted against major oxides (Fig. 4.15a) show similar patterns (S3A3, S3B1, S4B1 and S6A3) within the data set with the exception of CaO and Fe_2O_3. Harker diagrams of MnO, Th and Zn plotted against Fe_2O_3 (Fig. 4.15b) display strong positive or negative linear correlations. These correlations are supported by r^2 values of >0.7 (Everitt & Skrondal, 2010). Figure 4.15c displays Ba, Cs, Rb distributions across the twelve porphyry samples. These trace metals demonstrated similar patterns and outliers (S3A3 and S3B1). The two samples taken from the highly altered porphyry on the DP are displayed in red throughout the Figure 4.15 graphs. These appear to be the common outliers or one extreme in the linear correlations alongside the heavily weathered hyalodacite sample S4B1.

The spider diagram of the Berlins Porphyry REE plotted against a standard chondrite (Fig. 4.16) displays the largest amount of rare earth elements. All other spider diagrams plotted against varieties of OIBs and MORBs are incomplete due to a lack of data, but are included in the Appendix. The rare earth elemental data of the Berlins Porphyry exhibits a granodioritic signature with enriched light rare earth elements (LREE), depleted heavy rare earth elements (HREE) and a europium anomaly. These results highlight all the Berlins Porphyry samples that were analysed are geochemically related; however, sample S3A3 shows some geochemical diversity (Fig. 4.16).

Iron oxide (Fe_2O_3) weight percentages vary throughout the Berlins Porphyry and highlight site-based trends in abundance. The highly altered porphyry surrounding the iron concretions on the DP are the lowest percentage at 1.1-1.43% (Table 4.3). Unaltered Berlins Porphyry (type A, C & F) scattered throughout the LBG and DP displays the highest percentage at >2.95% and porphyry samples that surround the boulder-like structures in the LBG show intermediate weight percentages at 1.79-2.29%.

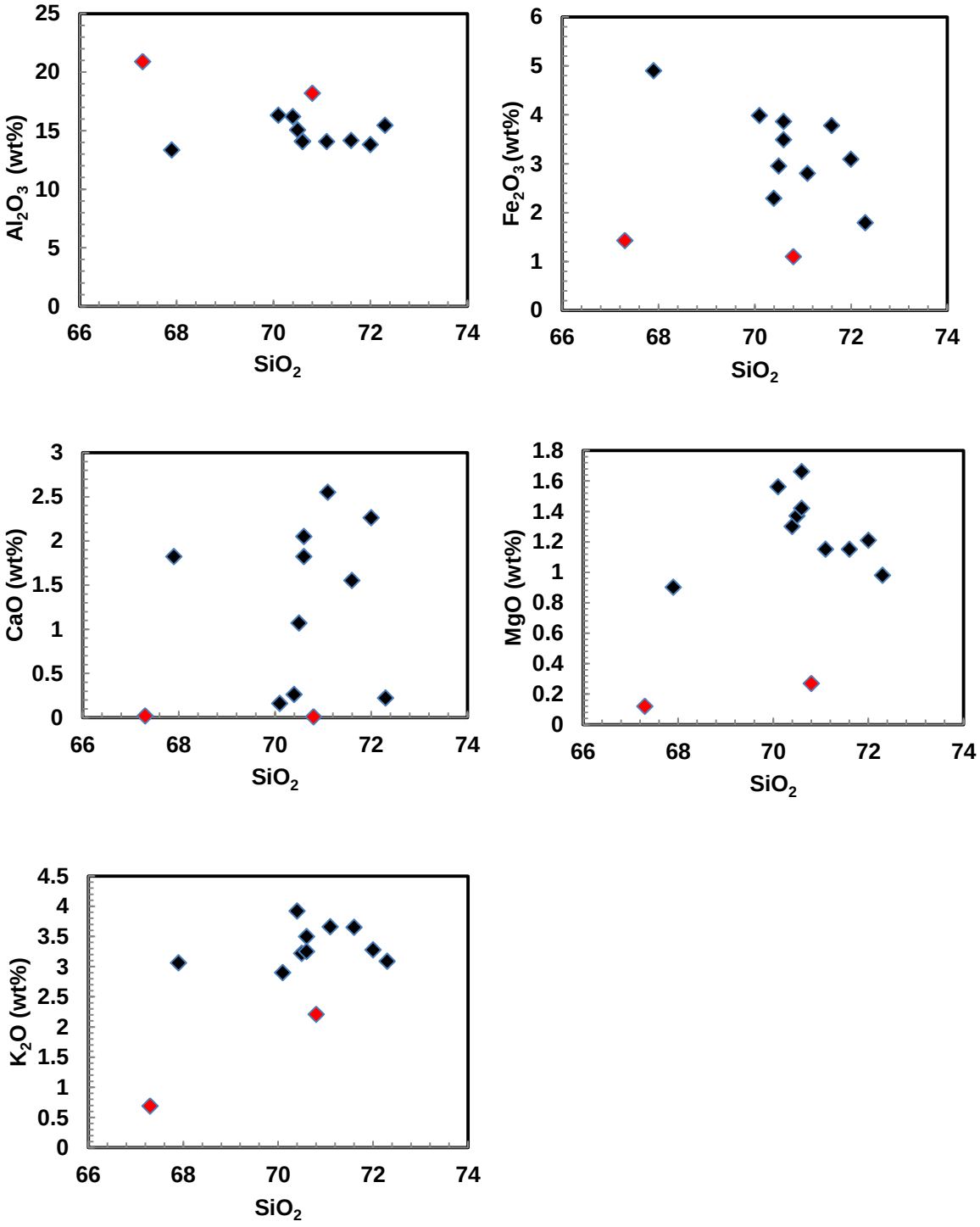

Figure 4.15a: Harker Diagrams of SiO_2 plotted against major oxides. The red symbols represent the two outliers, sample S3A3 and S3B1.

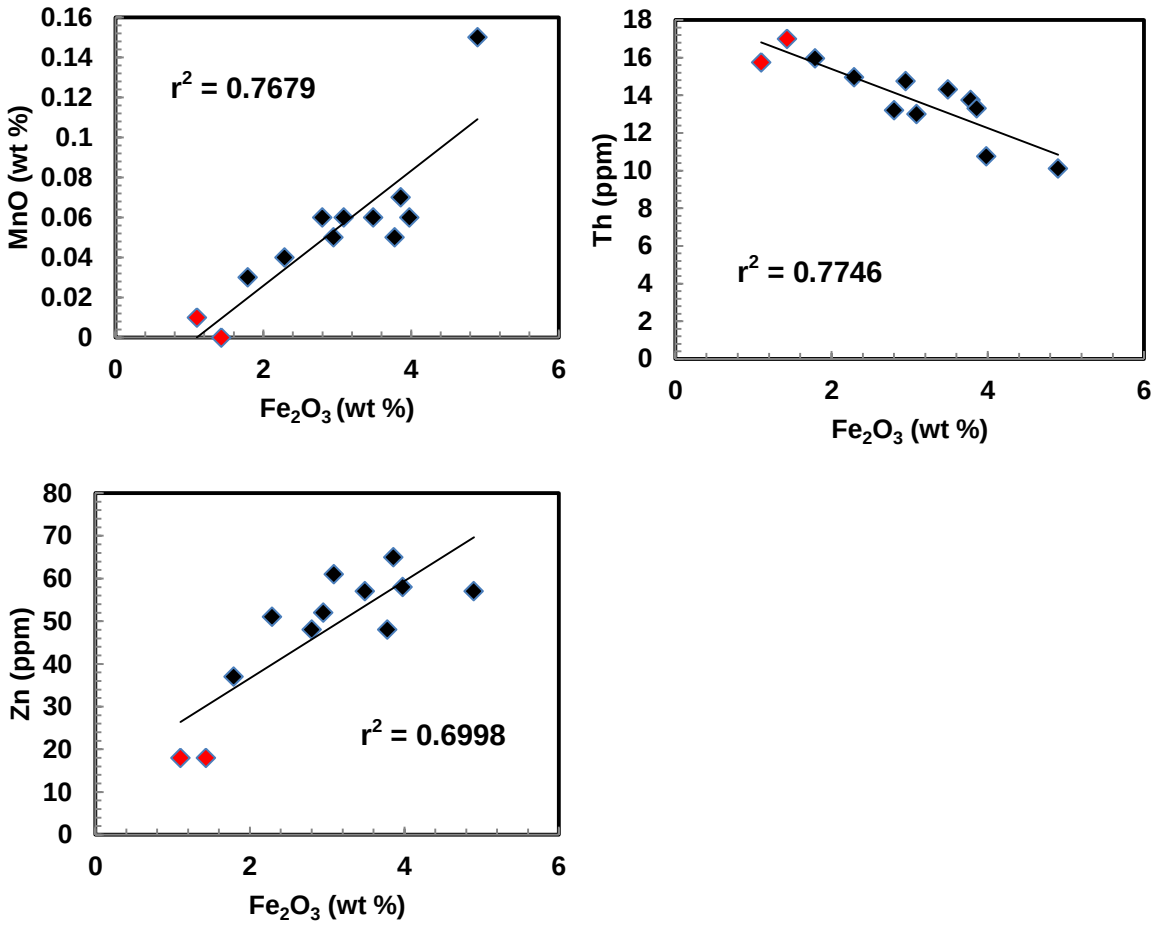

Figure 4.15b: Harker diagrams displaying Fe_2O_3 (wt%) plotted against MnO (wt%) Th (ppm) and Zn (ppm). The red symbols represent the two outliers, sample S3A3 and S3B1.

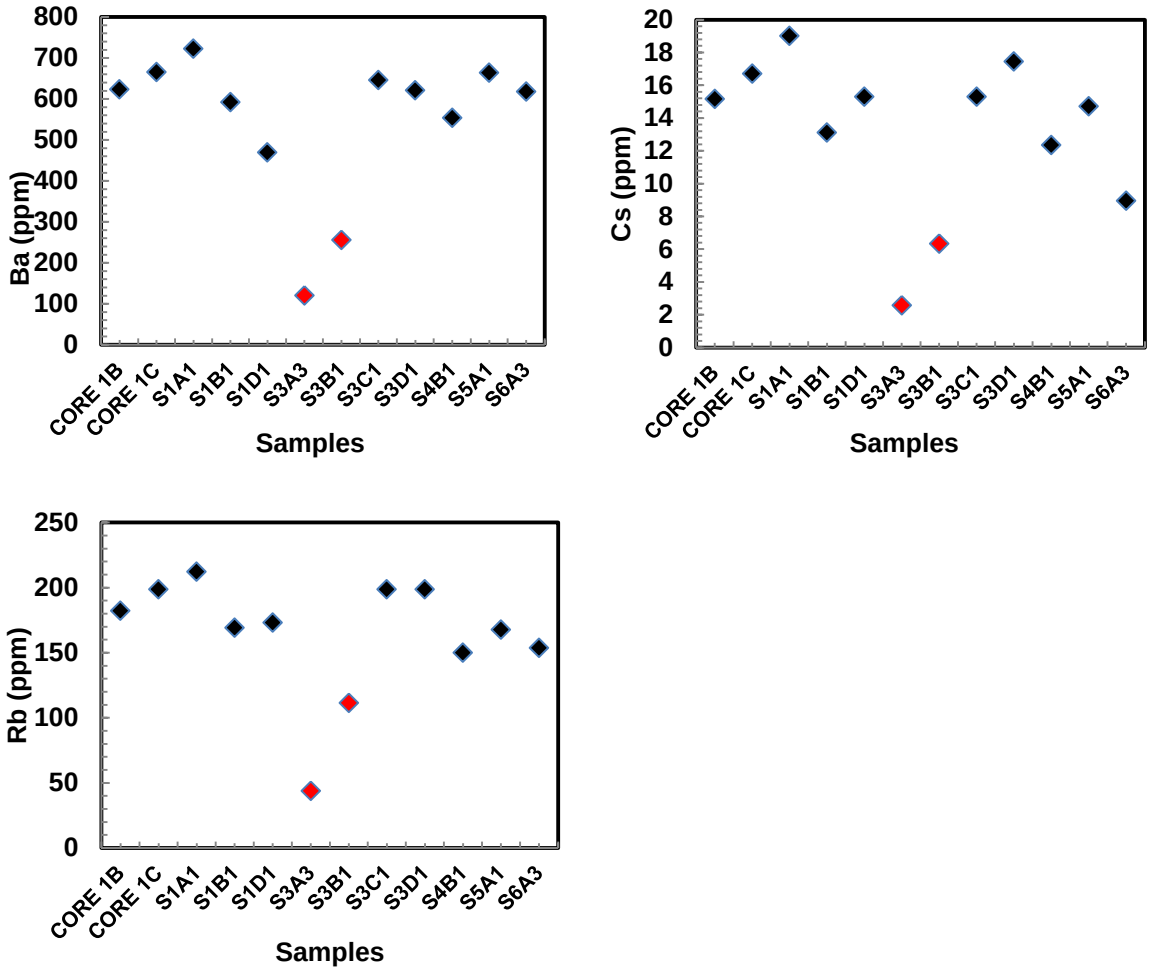

Figure 4.15c: Trend graphs showing Ba, Cs and Rb distributions for the twelve Berlins Porphyry samples. Samples S3A3 and S3B1 (red) are outliers within all plots.

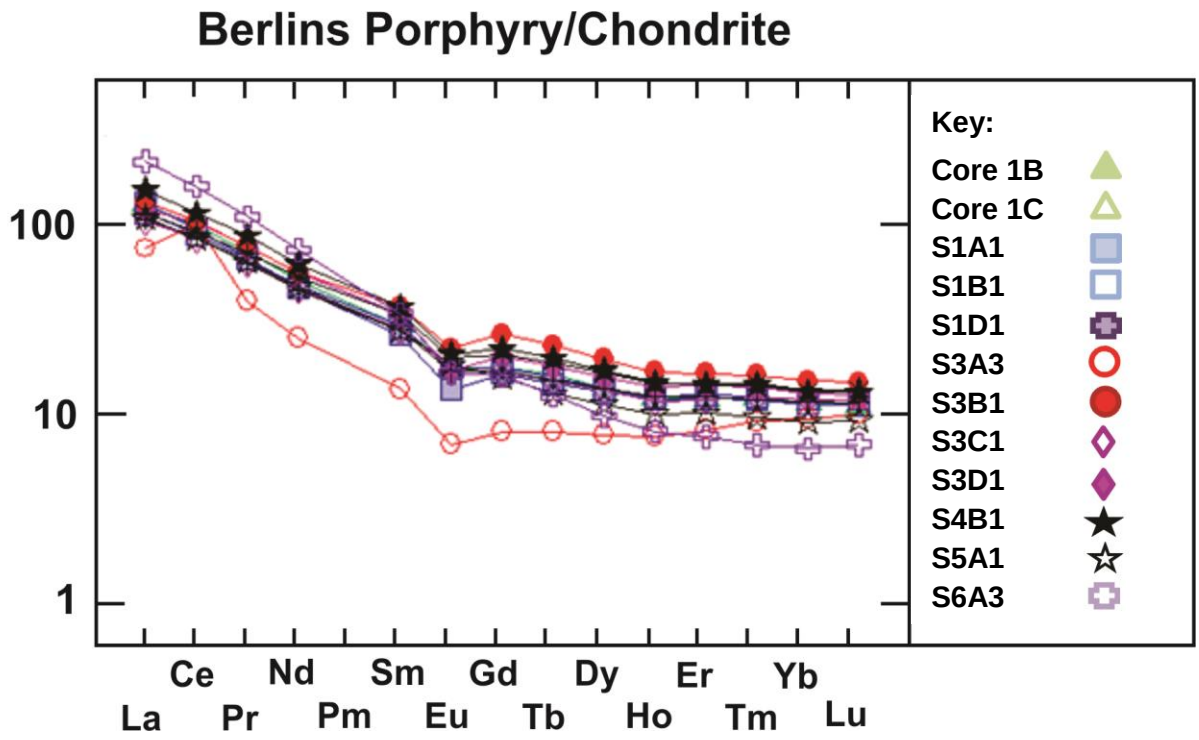

Figure 4.16: Spider diagram of Berlins Porphyry rare earth elements plotted against a standard chondrite rock. Sample S3A3 (red hollow circle) is geochemically diverse from the remaining porphyry samples. Promethium (Pm) was not included in the whole rock analysis data set and therefore, has no representation on this graph.

Table 4.3: Berlins Porphyry iron oxide percentages (Fe_2O_3 wt %) from whole rock analysis

Sample	Porphyry Type	Fe_2O_3 (wt %)	Sample Description
Core 1B	C	3.09	Unaltered Porphyry
Core 1C	A	2.8	Unaltered Porphyry
S1A1	E	2.29	Porphyry Surrounding Rounded Boulders
S1B1	C	2.95	Unaltered Porphyry
S1D1	A	1.79	Porphyry Surrounding Rounded Boulders
S3A3	G	1.43	Porphyry Surrounding Altered Iron Concretions
S3B1	G	1.1	Porphyry Surrounding Altered Iron Concretions
S3C1	A	3.78	Unaltered Porphyry
S3D1	A	3.86	Unaltered Porphyry
S4B1	B	4.9	Unaltered Porphyry
S5A1	A	3.49	Unaltered Porphyry
S6A3	D	3.98	Greenland Group + Berlins Porphyry

4.8 Carbon Isotope Analysis

Six samples analysed for carbon isotope signatures are shown below (Fig. 4.17) and one sample (S3B13B) shows both the preliminary and secondary drill locations. The carbon isotopic analysis includes the percentage of carbon within each pulverized rock sample and its $\delta^{13}C‰$ values.

The weight percentage of carbon within the iron concretions varies between each sample and across the three mineralization layers of sample S3B13B. Figure 4.18a shows minimal amounts of carbon (<0.11 wt%) in the altered porphyry centre, but a significant increase in carbon within the magnetite and hematite layer of sample S3B13B. This increase in carbon is reproduced three separate times including after being treated by H_2O_2 (section 3.412). After an acetic acid treatment on sample S3B13B minimal amounts of carbon are produced. Results from all of the iron concretions contain $\delta^{13}C‰$ values between -21‰ and -28‰ with all values in the magnetite layer below -25‰ (Fig. 4.18b). The average $\delta^{13}C‰$ value across all three mineralization layers is -26‰ ± 4‰. These results are also reproduced after treated with H_2O_2. Additionally, after an acetic acid treatment on sample S3B13B the average $\delta^{13}C‰$ value decreased to -27‰ ± 3‰.

Samples from Core 1A & B both show more carbon (wt%) and less negative $\delta^{13}C‰$ values when untreated. After H_2O_2 and acetic acid treatments a change in the weight percentage of carbon and the $\delta^{13}C‰$ values are evident (Table 4.4). The H_2O_2 treatment slightly decreases the weight percentage of carbon, but the acetic acid treatment shows a notable decrease in carbon. The $\delta^{13}C‰$ values remain similar after the H_2O_2 treatment, but after the acetic acid treatment all values decrease significantly. Overall, Core 1B shows the largest change after both the H_2O_2 and acetic acid treatments (Table 4.4).

Table 4.4: Carbon isotopic results of the unaltered porphyry samples

Sample	Porphyry	%C Initial	$\delta^{13}C$ Initial	%C H_2O_2	$\delta^{13}C$ H_2O_2	%C Acetic acid	$\delta^{13}C$ Acetic acid
Core 1A1	Type A	0.14279	-16.06	0.13213	-16.04	0.00005	-27.91
Core 1A2	Type A	0.14305	-15.89	0.11649	-16.97	0.00025	-32.13
Core 1A3	Type A	0.12057	-16.06	0.06988	-16.36	0.00008	-30.13
Core 1B1	Type **C**	0.57663	-13.00	0.49905	-13.08	0.00009	-29.64
Core 1B2	Type C	0.57604	-12.99	0.40575	-12.99	0.00017	-30.82
Core 1B3	Type C	0.58889	-12.86	0.56326	-12.87	0.00007	-30.06

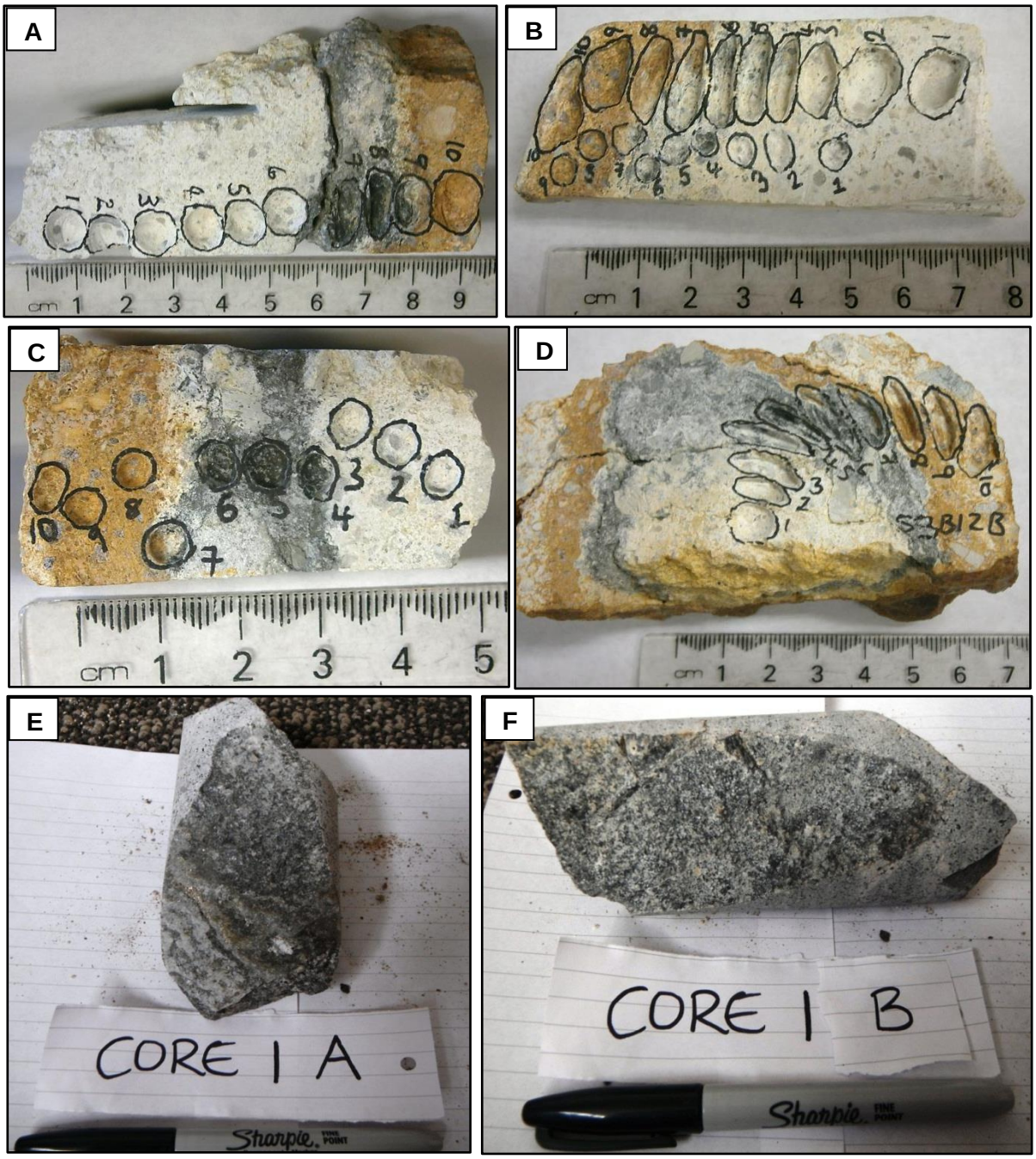

Figure 4.17: Cross-sections of samples S3B13D (A), S3B13B (B), S3B12C (C), S3B12B (D), Core 1A (E), and Core 1B (F) analysed for total carbon (wt%) and $\delta^{13}C‰$. Drill points are shown across the altered iron concretions and sample S3B13B shows both the preliminary and secondary points. The remaining samples were powdered for analysis.

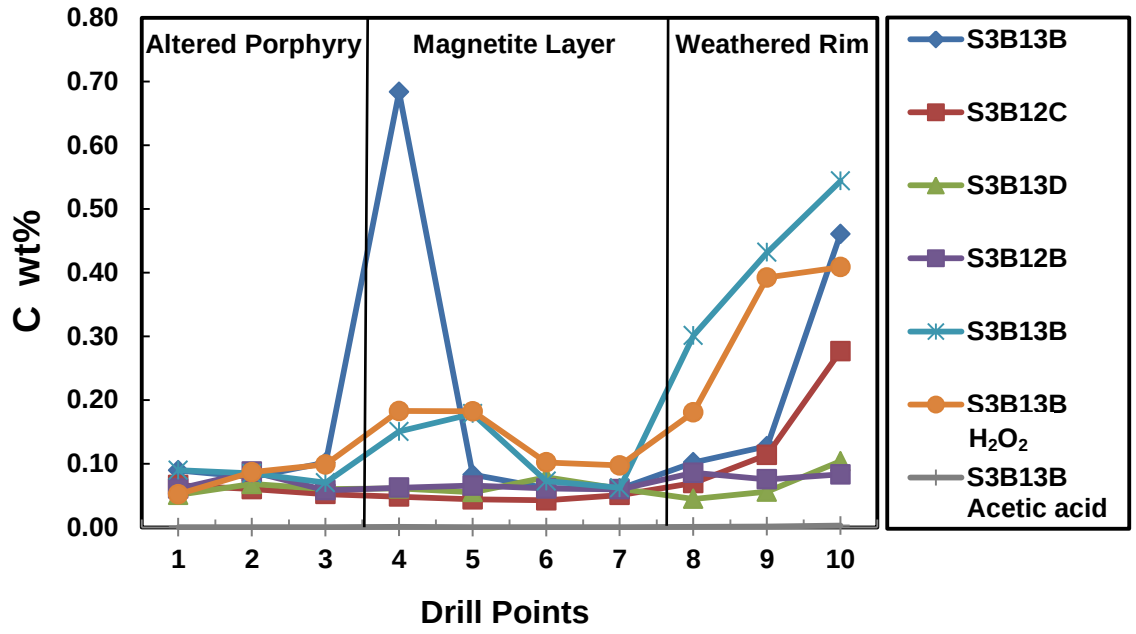

Figure 4.18a: Preliminary and secondary weight percentages of carbon (including samples treated with H_2O_2 and acetic acid) from two iron concretions (S3B12 and S3B13) within the altered Berlins Porphyry.

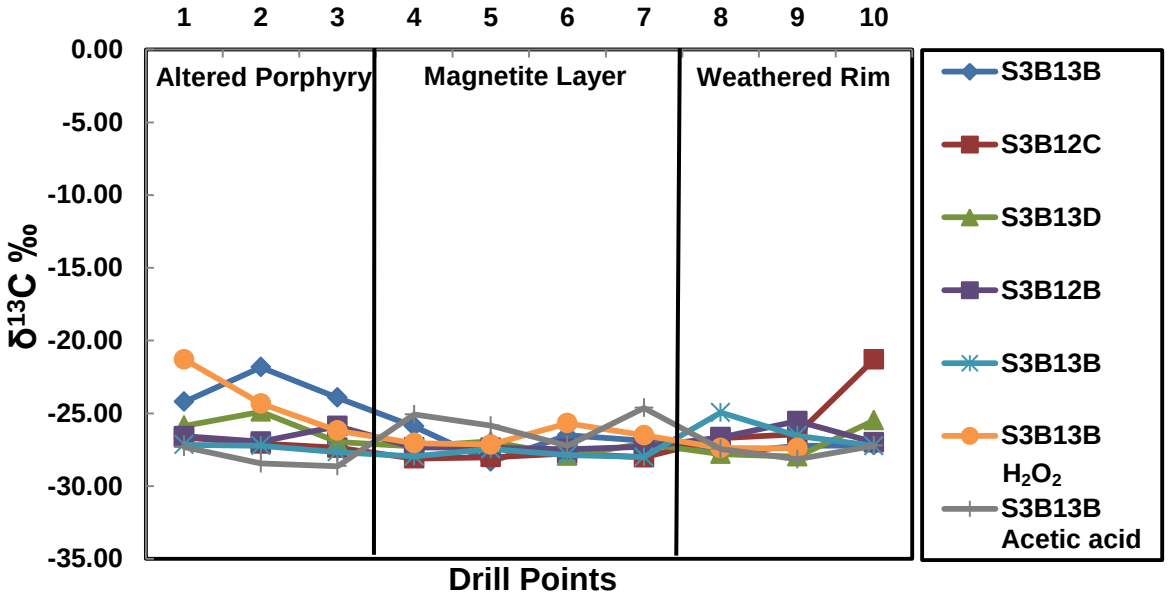

Figure 4.18b: The $\delta^{13}C$ (‰) values from the preliminary and secondary carbon isotope results of two iron concretions (S3B12 and S3B13) within the altered Berlins Porphyry.

Chapter Five – Discussion

5.1 Berlins Porphyry Emplacement

Porphyry systems experience a wide variety of magmatic and hydrothermal events during their formation. As a result, porphyry deposits comprise of a sequence of heterogeneous rocks hosting localized alteration zones and a wide range of textural features. The Berlins Porphyry displays mineralogical, textural and geochemical variations and is therefore, categorised into seven types. All Berlins Porphyry samples are linked by the presence of zoned primary resorbed quartz phenocrysts (Fig. 4.13 D & F) and a common zonation within the phenocryst indicates that they are source from the upper section of a large intrusion (Manhood et al. 1996). A general description and the emplacement history of each porphyry type are included below, not in alphabetical order.

Type A porphyry (Fig. 4.4) is a porphyritic quartz, plagioclase, biotite and xenolith-rich hyalodacite. Nathan (1974) suggests that the hyalodacite is the chilled outer margin of all Berlins Porphyry intrusions. However, the presence of broken phenocrysts, a glassy groundmass and Greenland Group xenoliths indicate that type A porphyry was emplaced during a higher energy phase. Over-pressured magmatic fluids within porphyry systems release and produce energy that shatters surrounding rocks. The product of this explosive emplacement is a plutonic magmatic-hydrothermal breccia (Sillitoe, 2010). The presence of marginal foliations within the glassy groundmass (Fig. 4.5 A) suggest that the intrusions remained hot and mobile after emplacement (Winter, 2010). Replacement textures in the form of sericitic (Fig. 4.5 B) and calcitic alteration indicates an increase in hydrothermal fluid migration. Both the marginal foliations and brecciated country rock indicate that type A porphyry formed on the outer edges of the Berlins Porphyry intrusions. Type B porphyry is another hyalodacite, but is sourced from deeper within the Berlins Porphyry intrusions. Here the magmatic-hydrothermal brecciation intensity is reduced resulting in no xenoliths and all phenocrysts, although shattered, remain in their original shape (Fig. 4.4 B). Further into the centre of the intrusions the crystals are able to grow to a medium-grain size and produce the type F porphyry. Nathan (1974)

postulates that this quartz, plagioclase, and biotite-rich microgranodiorite formed in mid-to-outer zones of the intrusions, and textural evidence supports this. The medium-grained crystals show cooling fractures and minor fragmentation from brecciation on the outer margins of the intrusions. Larger euhedral crystals containing no fragmentation are also found in the Berlins Porphyry and categorised as type C porphyry (Fig. 4.4). This coarse-grained quartz, plagioclase, biotite, and alkali feldspar-rich granodiorite formed in the centre of the Berlins Porphyry intrusions (Nathan, 1974). The rock cooled slowly and was sheltered from the hyalodacite's explosive emplacement.

Textural variations within the Berlins Porphyry are linked to the initial emplacement of the rock. Gradational cooling throughout the intrusions created a sequence of crystal sizes from a granodiorite to a microgranodiorite. The explosive emplacement in the outer margins of the intrusions created a wide variety of crystal morphologies and subsequent replacement alteration textures.

Secondary alteration is evident from geochemical analysis on the Berlins Porphyry. The slope of the rare earth elemental (REE) data (Fig. 4.16) and the high percentages of plagioclase feldspars (10-30 wt%), biotite (5-10 wt%) and SiO_2 (67-72 wt%) indicate the Berlins Porphyry samples are granodiorites (Bogaerts et al. 2003 & Winter, 2010). The europium (Eu) anomaly supports plagioclase fractionation, as Eu^{2+} act as a substitute for Ca^{2+} in calc-plagioclase feldspars (Winter, 2010), therefore, depleting within the melt during plagioclase crystallization. The geochemical variations identified by the REE's are represented by sample S3A3. This sample is highly altered and has undergone significant mineralogical and textural changes from the unaltered Berlins Porphyry samples.

Harker diagrams (Fig. 4.15) highlight additional hydrothermal alteration and weathering within the Berlins Porphyry. The majority of the Berlins Porphyry samples that were analysed are geochemically similar (Fig. 4.15a), but variations appear to be linked to the highly altered DP samples (S3A3 and S3B1) and the intensely weathered LBG sample (S4B1); (Fig. 4.15a-c). The highly altered samples are deficient in the trace metals Ba, Cs and Rb. Nesbitt et al. (1980) argues that low Ba, Cs and Rb are linked to a deficiency in low temperature weathering clays.

Further geochemical variations across all Berlins Porphyry samples are shown by the abundance of CaO and Fe_2O_3 (Fig. 4.15a). A series of CO_2-rich fluids injecting into the Berlins Porphyry

intrusions after emplacement and subsequently precipitating calcite mineralization may contribute to the CaO variation. The distribution of Fe_2O_3 within the Berlins Porphyry is related to both hydrothermal alteration and low-temperature weathering. Unaltered porphyry samples display high Fe_2O_3 wt% (Fig. 5.1) as the samples are abundant in primary magnetite and biotite. Conversely, porphyry samples adjacent to weathering in the LBG have lower percentages as the iron (hematite) concentrates around the rounded structures. Intensely weathered porphyry samples (S4B1) are represented by higher Fe_2O_3 wt% of 4.9%. The highly altered porphyry on the DP surrounding the iron concretions shows the lowest Fe_2O_3 wt% as all primary biotite and magnetite are replaced with kaolinite and muscovite, leaving the dissolved iron in solution. Lastly, sample S6A3 (type D porphyry) shows high Fe_2O_3 (3.98 wt%) due to the assimilation of the biotite-rich Greenland Group basement rock (Adams, 2004); (Table 4.1). Additional to magnetite crystallization, evidence suggest manganese and zinc are also crystallizing (Fig. 4.15b). It is common for iron (Fe) and manganese (Mn) to precipitate together in hydrothermal systems (Hein et al. 1997) and zinc (Zn) can incorporate in the crystal lattices of iron oxide minerals (Hedenquist & Lowenstern, 1994). In contrast, thorium (Th) shows a negative linear relationship with Fe_2O_3 (Fig. 4.15b) as it preferentially leaches out during weathering processes (Braun et al. 1993).

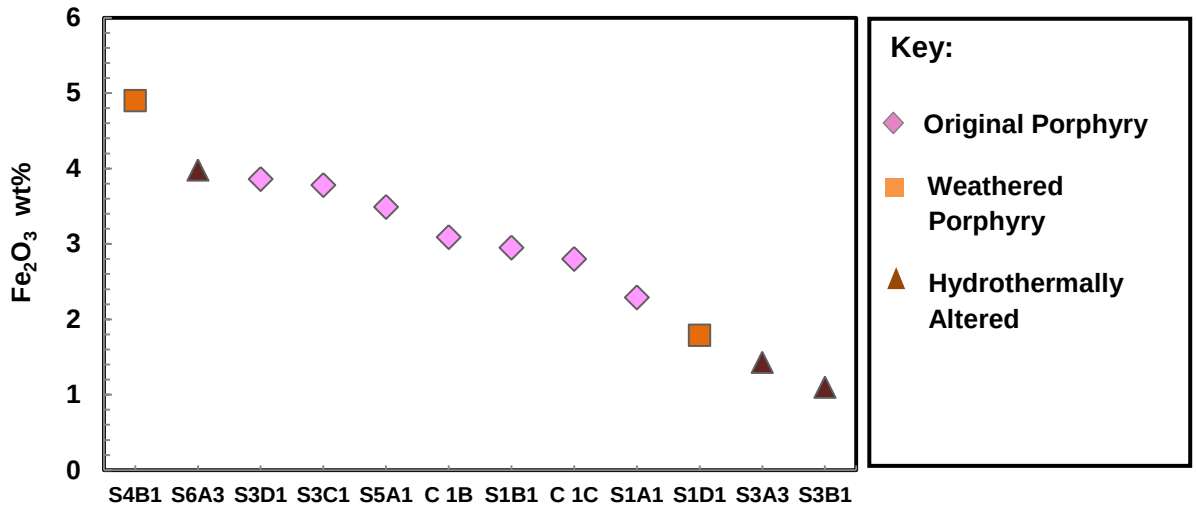

Figure 5.1: Iron oxide percentages that display a link to alteration within the Berlins Porphyry. Samples in pink represent original porphyry containing primary magnetite and biotite, samples in orange are related to weathering and samples in brown are related to hydrothermal activity and assimilation.

5.2 Hydrothermal Alteration within the Berlins Porphyry

Heterogeneity within the Berlins Porphyry is created by a variety of factors including hydrothermal activity and low-temperature weathering. Hydrothermal alteration occurred during and/or after the porphyry's emplacement. Subsequent uplift, exposure and erosion contributed to low-temperature weathering processes.

Propylitic hydrothermal alteration is a common alteration style that occurs within mid-to-outer zones of porphyry systems. This alteration is produced by the injection of iron, CO_2 and sulphur-bearing hydrothermal fluids into a porphyry system. Typical alteration mineralogy includes calcite, sericite, pyrite, chlorite and iron oxides (Parry & Downey, 1982; GACMDD, 1996). The Berlins Porphyry hyalodacite and granodiorite (types A & C) displays evidence of this type of alteration. They host secondary calcite that replaces primary calc-plagioclase feldspars (Fig. 4.6 A) and cross-cuts mineralization as calcitic veins (Fig. 4.6 B). This indicates at least two phases of CO_2-rich fluid injections within the porphyry system (GACMDD, 1996). Additionally, small amounts of sericitic alteration on the primary feldspars (Fig. 4.5 B) and pyritization of the primary magnetite within the Berlins Porphyry suggest a short-lived injection of sulphur-rich fluids (GACMDD, 1996). Lastly, the replacement of primary igneous biotite with chlorite and magnetite supports the presence of propylitic alteration within the Berlins Porphyry.

Supplementary hydrothermal alteration is evident within the Berlins Porphyry at site 6 (Type D porphyry), where a mingled contact with the basement Greenland Group rock indicates localized assimilation. The presence of recrystallized quartz and biotite veins, micro-deformed biotite crystals, and an overall foliation to the rock are evidence of assimilation and fluid alteration (Winter, 2010). Xenoliths of the basement Greenland Group rock are limited as they have combined with the Berlins Porphyry rock at this site. The rare earth elemental (REE) data suggests this porphyry is geochemically similar to other Berlins Porphyry (Fig. 4.16), but major oxides CaO and Fe_2O_3 highlight an alteration event. These major oxides can be linked to the precipitation of additional biotite crystals and dissolution of calc-plagioclase feldspars during the assimilation process.

Furthermore, a localized and highly altered type A porphyry is present on the DP at sites 3A and B. Type A porphyry is located at the outer margins of the Berlins Porphyry intrusions and is exposed to hydrothermal alteration, evident from both sericitic and calcitic alteration (Fig. 4.5 B; Fig. 4.6 A). The type of hydrothermal alteration that created this highly altered type G porphyry is low in sulphides. This porphyry displays geochemical variations from the original Berlins Porphyry and compositionally hosts primary quartz phenocrysts, biotite relics, magnetite and secondary hydrothermal mineralization. Petrographic analysis identified the presence of igneous and biomineralized magnetite (Section 5.41), recrystallized quartz, and muscovite/sericite. Additionally, XRD analysis identified kaolinite and sanadine and EM and EDS analysis confirmed the presence of a alkali feldspar and pyrite through potassium, aluminium, iron and sulphur elemental signatures (Fig. 4.12).

The type of alkali feldspar present within this rock is difficult to determine; however, textural analysis demonstrates it interlocking with recrystallized quartz (Fig. 4.12 B). This implies the alkali feldspar is a secondary hydrothermal mineral such as adularia (Dong & Morrison, 1995), rather than sanadine. If sanadine was present within this highly altered rock, its formation temperature would be >525°C (Goldsmith & Laves, 1954), which exceeds the temperature range (200-250°C); (Fig. 5.3) of this localized low-sulphidation hydrothermal system.

Pyrite that is present within this highly altered porphyry is restricted to the replacement of biomineralized magnetite crystals (Fig. 4.12 A). Whole rock and petrographic analysis of this altered Berlins Porphyry shows an overall depletion in sulphides; however, pyritization within this highly altered rock is found only in exposed magnetite nodules. The source of the sulphur is then related to meteoric fluid migration, through leaching of the unconformably overlying Brunner Coal Measures.

The presence of kaolinite and muscovite in place of biotite, chlorite, and magnetite (Fig. 4.11 C & D) highlight the systems slow depletion of iron-bearing minerals. Biotite altering to kaolinite demonstrates this alteration process and the subsequent release of cations, K^+ and Fe^{2+} into solution. Biotite altering to muscovite demonstrates the use of the K^+ cation in solution, but the Fe^{2+} cation preferentially remains in solution as shown in the two reactions below.

$$2KFe_3AlSi_3O_{10}(OH)_2 + 14H^+ \leftrightarrow Al_2Si_2O_5(OH)_4 + 2K^+ + 6Fe^{2+} + 4SiO_2 + 7H_2O$$

(biotite) *(kaolinite)*

$$2KFe_3AlSi_3O_{10}(OH)_2 + 12H^+ \leftrightarrow 2KAl_2Si_3O_5(OH)_4 + 6Fe^{2+} + 6H_2O$$

(biotite) *(muscovite)*

Iron depletion in this highly altered rock is supported through whole rock analysis (Table 4.3), but thermodynamics indicates that dissolved iron in this hydrothermal system at depths of ~2km oxidises to magnetite as shown in the reaction below and in Figure 5.2.

$$3Fe^{2+} + 3H_2O + \tfrac{1}{2}O_2 \leftrightarrow Fe_3O_4 + 6H^+$$

All magnetite mineralization is confined to the iron concretions within this altered porphyry. This suggests iron oxidation was favourable in these concretions.

Overall, mineralization within the white altered porphyry (type G); (Table 4.1) indicates the rock formed in either an epithermal or mesothermal hydrothermal system (GACMDD, 1996) at ~2km depth. Kaolinite is identified as the lowest temperature mineral and typically crystallizes in hydrothermal systems from 100°C to 200°C (Inoue, 1995). However, the kaolinite crystallization in this rock is contemporaneous with muscovite crystallization (Fig. 4.11 D). Muscovite crystallizes at 200 to 700°C in these types of hydrothermal systems (Inoue, 1995; GACMDD, 1996 & Deer et al. 2004), which increases the minimum temperature of this hydrothermal system to ≥200°C (Inoue, 1995).

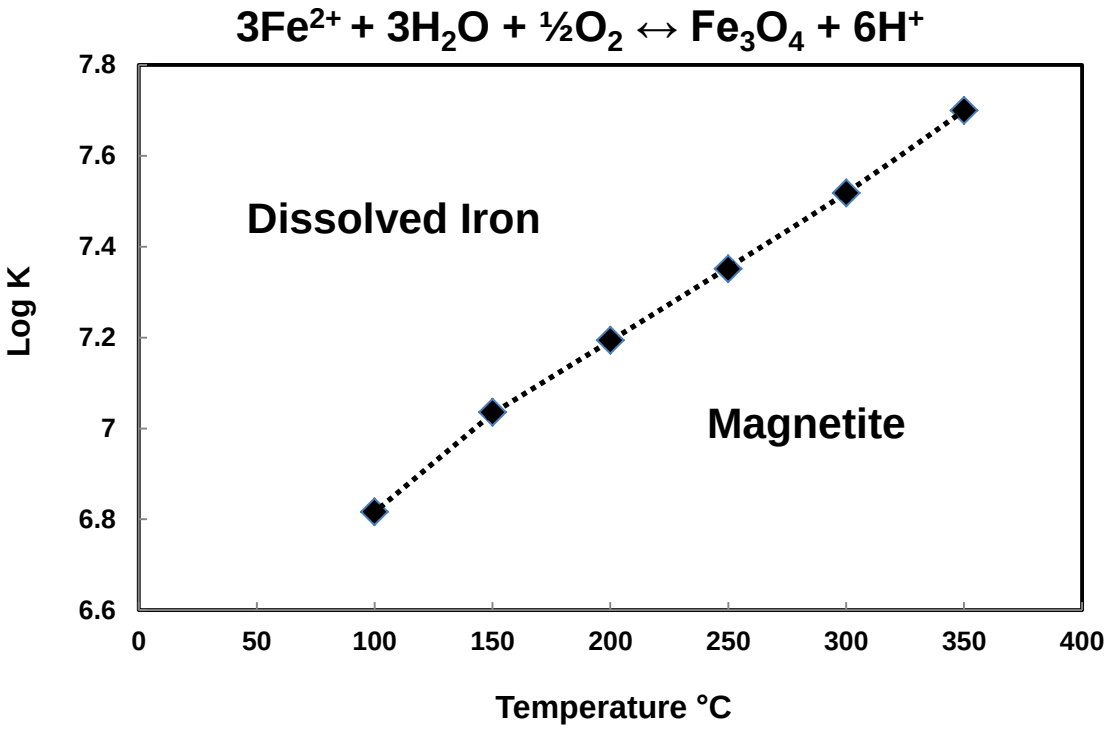

Figure 5.2: A log activity graph for dissolved iron oxidising to magnetite at 2kms depth (600bars pressure). This reaction is favourable as Log K is positive. The reaction is shown above and calculations were made using SUPCRT (Shock, 1998).

5.3 Modern Weathering of the Berlins Porphyry

The LBG Berlins Porphyry samples are heavily weathered due to their exposure to rivers, extensive vegetation and the high amount of rainfall in the region. Type E porphyry represents a weathered hyalodacite abundant in hematite and clay minerals. The hyalodacite porphyry preferentially weathers when compared to granodiorite porphyry as it is both fine-grained and contains volcanic glass. Additionally, large exposures of granitic bodies are susceptible to spheroidal weathering as jointing increases weathering at corners and shapes granitic rocks into rounded boulder-like structures or spheroids (Ollier, 1971). These boulders are often surrounded by deformed layers of hematite and clay (Blackwelder, 1925; Røyne et al. 2008). Site 1D, in the LBG hosts these boulder-like structures and surrounding weathered clay and hematite-rich layers.

5.4 Microbial Activity in the Berlins Porphyry

The Berlins Porphyry emplaced at ~2km depth within the crust and subsequently uplifted and exposed. An extremely rare exposure of well-preserved and highly altered porphyry on the DP has uncovered Fe-rich concretions/nodules. These structures host three mineralization layers; an altered porphyry centre, followed by a magnetite layer and an outer weathered rim predominantly comprised of hematite. The hematite mineralization replaces all previous mineral morphologies, including the magnetite mineralization, by encrusting over each crystal's surface. The recent exposure of the iron concretions has allowed the magnetite mineralization to slowly weather to hematite, but it has effectively protected an inner magnetite layer from modern erosion. Both the deficiency of iron in the surrounding hydrothermally altered rock (Fig. 5.1) and the high abundance of magnetite that crystallized into these Fe-rich concretions imply secondary catalyzation.

These iron concretions are geologically rare as they display no specific point or nucleus to drive the large amount of magnetite precipitation (Martin & Bils, 1964), however, bacteria are catalysts for the formation of concretions/nodules (Douka, 1977; Ghiorse & Hirsch, 1982; Pye et al. 1990; Wang et al. 2008; Templeton & Knowles, 2009). This could suggest the presence of ancient microbial activity within a highly altered unit of the Berlins Porphyry. Additionally, these concretions appear

morphologically and mineralogically comparable to concentrated mineralization that forms in modern hydrothermal systems (Ghiorse & Hirsch, 1982, Palumbo et al. 2001; Miyata et al. 2007; Wang et al. 2008).

5.41 Evidence of Microbial Activity

Six criteria were used to identify the presence of microfossils within the Berlins Porphyry, *Section 2.4*. The obtainable evidence for the presence of microfossils within the magnetite layer of the Berlins Porphyry iron concretions is discussed below.

The iron concretions and associated microbial activity are sourced from an ancient hydrothermal system. Hydrothermal systems are common environments to host microorganisms (Juniper & Fouquet 1988; Stetter, 1999; Rasmussen, 2000; Al-Hanbali & Holm, 2002; Amend et al. 2003), though to date, no microorganisms have been identified in deep-seated porphyry systems. These systems host areas of decreased temperatures and hydrothermal activity and provide microorganisms with the same mineral-enriched fluids that shallow hydrothermal system possess.

Microfossil structures within the magnetite layer of the iron concretions are represented by filaments, tubular hollows and spherical depressions. The filamentous structures (Fig. 4.10 A & B) are interpreted as rare branching filamentous microfossils within the Berlins Porphyry. This morphology is largely common for microorganisms in both ancient and modern hydrothermal systems (Awramik et al. 1983; Juniper & Fouquet, 1988; Ivarsson et al. 2008; Staudigel et al. 2008; Ivarsson et al. 2011; Templeton, 2011).

The tubular hollows that host rounded magnetite crystals and exist as interconnected networks throughout the primary quartz phenocrysts (Fig. 4.10 C-E) potentially indicate the presence of ancient tubular burrows, produced by the filamentous microorganisms. The ability for the microorganisms to burrow into quartz crystals requires an increase in temperature. Quartz crystals in standard state conditions (25°C/1bar) are stable, extremely hard and particularly difficult to burrow into. An increase in temperature decreases the stability of quartz crystals and therefore, the ability to burrow becomes less resistant. Often these burrows are partially angular and host earlier phases of muscovite or recrystallized quartz. This suggests the microorganisms may have utilized previous hydrothermally-

produced crystal fractures as burrowing pathways. At higher temperatures these pathways would be the most unstable part of a crystal and the path of least resistance. Cathodoluminescence images identify two types of burrows, successful burrows and abandoned or unsuccessful burrows. The successful burrows are shown as well-formed rounded shapes (Fig. 4.13 D & F) containing microcrystalline biomineralization. These burrows required protection from the hydrothermal system to be successful. The protection is accomplished through the presence of small feeder cracks (<2µm in diameter) as the only link to the active hydrothermal system. Larger feeder cracks caused an overexposure to the hydrothermal system and the failure of burrows. This is evident through poorly developed or angular burrows (Fig. 4.13 D) hosting no biomineralization. Furthermore, the abandoned burrows are 'healed' by a final quartz crystallization phase in the hydrothermal system (Bernet, 2005).

The spherical depressions hosting biomineralization and linked through a 'network of burrowing pathways' (Fig 4.10 E) can be interpreted as potential living chambers/cavities for the microorganisms. The shape of these structures are similar to previous resorbtion textures within the primary quartz phenocrysts, suggesting they may have been protected areas for the microorganisms in this hydrothermal system. Previous research identifies microbially induced mineral dissolution as a mechanism for burrowing at hydrothermal mounds (Al-Hanbali & Holm, 2002). Additionally, the stability of quartz decreases with increasing temperatures suggesting it is possible for these microorganisms to burrow into quartz crystals.

Other structures within this rock include the presence of segementation within the filamentous microfossils (Fig. 4.10 B). Preserving these features in a highly altered rock is challenging as hydrothermal systems experience pulses of activity that may erase such evidence. Conversely, the segmentation within these microfossils may be fractures that formed during heightened hydrothermal activity. The absence of cell wall material and segmented septae on the microfossils in this altered rock does not discount the presence of life. The microfossils themselves are rare and the more prevalent tubular burrows could not preserve such features.

Supplementary to biogenic features, chemical signatures of life were identified through the carbon isotopic analsysis. The focus of these analyses were on the iron concretions, but two unaltered core samples were additionally analysed. Carbon weight percentages within the iron concretions vary

across the mineralization layers. Sample S3B13B exhibits an increase in carbon across both the magnetite and hematite layers of the iron concretion, which was reproduced after the removal of modern organic contaminants via a H_2O_2 treatment. The remaining three iron concretion samples display minimal amounts of carbon across all three layers. This lack of carbon can be associated with a 'nugget effect' or the localized dispersal of carbon within the iron concretions. The $\delta^{13}C‰$ values show consistent results, where all four iron concretion transects have values in the range of organic carbon (Table 5.1). All calculated values across the three mineralization layers are below -21‰ with an overall average of -26‰ ± 4‰ (Fig 4.17c). The acetic acid wash decreased the $\delta^{13}C‰$ values (averaging -27‰) in every iron concretion sample indicating that carbonates are minimally affecting the carbon density in the iron concretions.

Table 5.1 $\delta^{13}C$ values across various reservoirs (Sharp, 2007)

Reservoirs	**Average $\delta^{13}C$ Ranges (‰)**
Organic carbon	(-23) – (-30)
Atmosphere	(-6) – (-7)
Continental silicic crust	(-6)
Carbonates	0 – 1
Mantle	(-5) – (-6)

The examination of carbon within the unaltered Berlins Porphyry samples, cores 1A & B additionally show evidence of life. The $\delta^{13}C‰$ values for the untreated and H_2O_2 treated samples are less negative than the iron concretion samples (averaging -14.5‰); (Table 4.4). After the removal of carbonates within the porphyry samples the $\delta^{13}C‰$ values decrease substantially to an average of -30‰ ± 2‰ (Table 4.4). Core 1B (granodiorite porphyry) shows the largest change after an acetic acid wash as the granodioritic samples host large amounts of calcite (1-5%); (Table 4.1). This is supported by the decrease in carbon by mass for all the core 1B samples after the acetic acid treatment. Calcite has a positive $\delta^{13}C‰$ value of 0-1‰ (Sharp, 2007), which causes the less negative $\delta^{13}C‰$ values in the core samples prior to its removal.

The percentages of organic carbon within the outer hematite rim are notable (Fig. 4.18a) and may be sourced from a variety of origins. The hematite layer of sample S3B13B shows similar weight percentages of carbon to the magnetite layer, suggesting the carbon in the hematite rim is sourced

from the hematite encrusted biomineralized magnetite crystals. Alternatively, the rounded globular hematite clusters (Fig. 4.10 F) could represent the presence of recrystallized modern microbial cells. Cabral et al. (2012) concludes spherical and botryoidal hematite aggregates (globular clusters) form from the replacement of microbial cells within sub-surface low-temperature weathering environments. The genetically identical clusters may serve as nuclei for hematite mineralization (Ferris et al. 1986; Templeton & Knowles, 2009). Moreover, organic carbon signatures within the weathered rim may be sourced from leached material of the unconformably overlying Brunner Coal Measures.

The organic carbon from the magnetite layer of the iron concretions can be linked to the microfossils and tubular burrows of that layer. The microfossils, the burrows and the magnetite formed during the hydrothermal system that produced the highly altered hyalodacite (Type G porphyry). Microfossils cross-cutting hydrothermal mineralization (Fig. 4.10 A & B) and recrystallized quartz in-filling tubular burrows (Fig. 4.13 D & F) signifies the presence of a hydrothermal system before and after microbial activity. Furthermore, the organic carbon within the magnetite layer is locked within the magnetite mineralization as an H_2O_2 treatment didn't remove the organic carbon within sample S3B13B.

The magnetite mineralization is morphologically specific within the tubular burrows and living cavities of the iron concretions. These morphologies include rounded cubic and hexagonal crystals (Fig. 4.9 C & D; Fig. 4.10 C), which only form with the interaction of microorganisms (Sparks et al. 1990) and are categorised as biomineralization. Tubular burrows without biomineralization (Fig. 4.10 D) can be explained as unsuccessful burrows caused by either extended exposure to the hydrothermal system or a limited amount of dissolved iron. It is unclear whether this biomineralization formed through intracellular or extracellular crystallization. Textural evidence shows extracellular crystallization as the crystals are not uniform in shape and display a range of sizes (Sparks et al. 1990); (Fig. 4.9 D). However, the presence of magnetite chains is indicative of intracellular crystallization (Fig. 4.9 C & D). Overall, there is not enough evidence to suggest either extracellular or intracellular crystallization, which can be attributed to a lack of the biogenic features preserved within the highly altered iron concretions.

The ancient microorganisms within the iron concretions display poor evidence for colonies or communities; however, the high abundance of biomineralization and an extensive networks of tubular burrows indicates the presence of an ancient microbial community. The lack of microfossils colonies preserved in the iron concretions may be due to the thickness of the thin sections. Ivarsson (2006) discusses the advantages of identifying microbial colonies within thick thin sections; "bacteria filaments in a colony occur at different focal depths within the thin section". Alternatively, the lack of microfossils can also be an artefact of poor preservation, but does not discount their existence in this highly altered rock.

5.42 Implications

The presence of microfossils in a highly altered section of the Berlins Porphyry is evidence for a new geologic system to sustain life. This localized low-sulphidation deep-seated hydrothermal system would have provided the geochemical conditions required for microbial growth. The ability for the microorganisms to potentially burrow into quartz phenocrysts allows them protection from the harsh environmental conditions of a porphyry system, whilst utilizing readily available dissolved iron. This continuous supply of dissolved iron was possible through the replacement of biotite with kaolinite and muscovite in the hydrothermal system. Thermodynamics shows dissolved iron in this hydrothermal system favours oxidation and the precipitation of magnetite. This provided the microorganisms with a sustainable niche, where they manipulated the iron's electron transfer as an energy source.

Difficulties remain when determining which phase of the hydrothermal system the microorganisms survived in; the system experienced pulses of hydrothermal activity and temperature variations. Figure 5.3 presents the temperature ranges of the hydrothermal system related to the mineralogy present within the rocks (excluding the weathered hematite rim). During the active phases of the hydrothermal system, the minerals precipitated at specific temperature ranges. When all the alteration minerals within this altered porphyry are plotted together a temperature range of 200-250°C is derived. This signifies the lowest temperature of the hydrothermal system in which the microorganisms survived is 200°C and the highest temperature is 250°C.

The microorganisms may have flourished in a lower activity phases of the hydrothermal system, where temperatures could have decreased below 200°C, but the only hydrothermal minerals that fall below 200°C are adularia and kaolinite. Energy dispersive X-ray spectroscopy shows adularia crystallizing alongside recrystallized quartz, suggesting a crystallization temperature >250°C. Electron microscopy highlights kaolinite crystallized simultaneously with muscovite (Fig. 4.11 D), indicating a minimum hydrothermal temperature of ~200°C. The microorganisms had to be actively precipitating biomineralized magnetite during the crystallization of kaolinite and muscovite as dissolved iron was being released during this process.

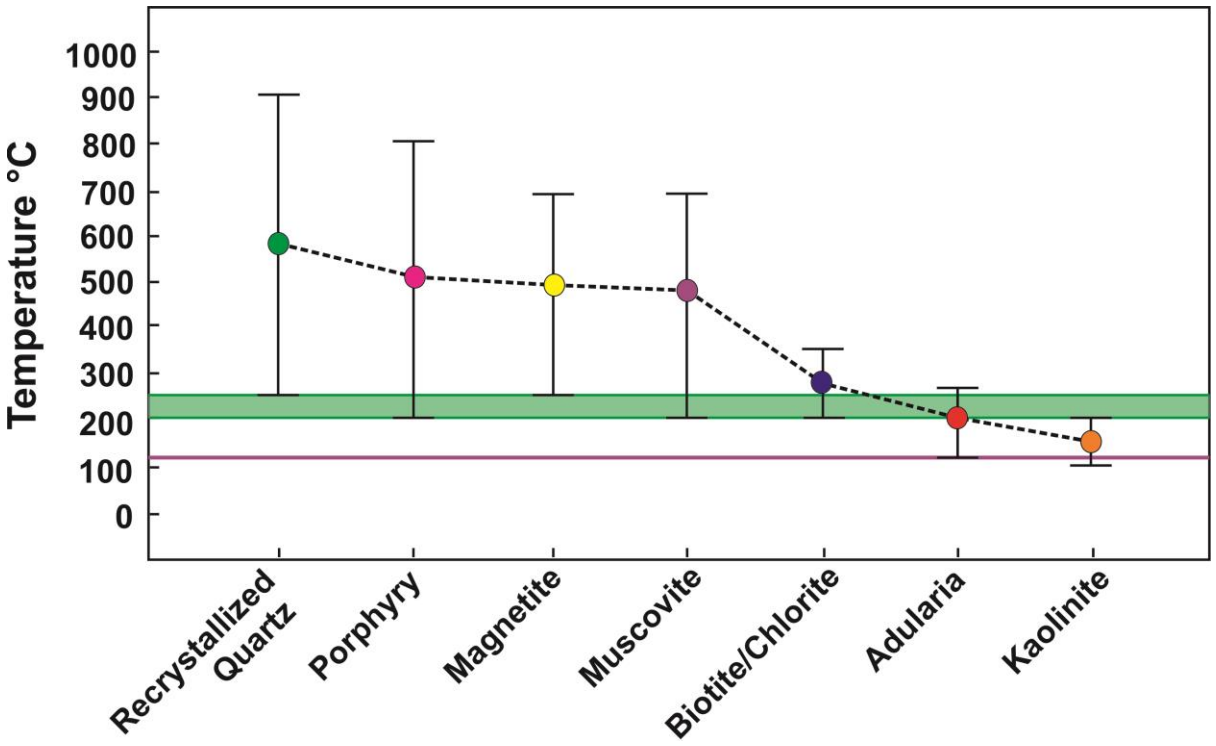

Figure 5.3: Crystallization temperatures of the mineralogy present within the Berlins Porphyry iron concretions. Recrystallized quartz forms from 250-900°C (Raleigh, 1965; Stipp et al. 2002). Porphyry systems range from 200-800°C (Sillitoe, 2010; Nathan, 1974). Igneous magnetite crystallizes from 250-650°C (Heider, 1987; Arancibia & Clark, 1996). Muscovite/sericite forms from 200-700°C (Inoue, 1995; GACMDD, 1996; Deer et al. 2004). Biotite altering to chlorite occurs at 200-340°C (Parry & Downey, 1982; Eggleton, 1985). Adularia crystallizes from 120-265°C (Steiner, 1970; Munha et al. 1980; Dong & Morrison, 1995). Kaolinite in hydrothermal system forms from 100-200°C (Inoue, 1995; GACMDD, 1996). The blue dotted line represents each minerals average crystallization temperature and shows a decreasing trend in the hydrothermal system. The purple line represents the temperature of the highest recorded microorganism, strain 121 and the green zone shows the temperature range of the microorganisms within the Berlins Porphyry iron concretions.

Chapter Six – Conclusions

The Berlins Porphyry is a series of heterogeneous intrusions comprised of magmatic hydrothermal breccia (type A – hyalodacite), to a partially brecciated microgranodiorite (type F), to a granodiorite (type C) and to a series of weathered and hydrothermally altered rocks. Alteration within the Berlins Porphyry includes propylitic alteration, contact fluid alteration/assimilation (type D), spheroidal weathering and low-sulphidation hydrothermal alteration. Geochemically the Berlins Porphyry rocks are relatively similar based on mineralogy and bulk geochemistry. The one potential exception is the hydrothermally altered rock (type G) on the Denniston Plateau, where it has experienced greater hydrothermal alteration. Additionally, within this highly altered unit are iron concretions that are compositionally, texturally and geochemically diverse from all other Berlins Porphyry.

The iron concretions—specifically the magnetite layer—indicate a microbially mediated formation. The Berlins Porphyry clearly demonstrates five out of the six criteria indicative of microbial life. The lack of colonial or community evidence can be linked to the challenge of preserving microfossils in a hydrothermally altered rock. The results that indicate the presence of life within the iron concretions cannot be explained by any other geological processes and therefore, they can be interpreted as putative microfossils and microbial activity within an ancient porphyry system.

This ancient system has since uplifted and become exposed at the surface, providing a glimpse of deep-seated porphyry processes. The rare preservation of the localized and intensely altered rock and the iron concretions has created an opportunity to investigate the potential for life in deep-seated porphyry systems. These ancient microorganisms have demonstrated an ability to mediate the precipitation of magnetite in temperatures exceeding 200-250°C. Life identified in these environments aids in the investigation of how life evolved on our planet and the potential for life to colonize other planets.

Chapter Seven – References

Adams, C.J.D., & Nathan, S. (1978). Cretaceous chronology of the Lower Buller Valley, South Island, New Zealand. *New Zealand Journal of Geology and Geophysics*, 21(4), 455–462.

Adams, C.J.D. (2004). Rb-Sr age strontium isotope characteristics of the Greenland Group, Buller Terrane, New Zealand, and correlations at the East Gondwanaland margin. *New Zealand Journal of Geology and Geophysics*, 47, 189–200.

Al-Hanbali, H.S., & Holm, N.G. (2002). Evidence for fossilized subsurface microbial communities at the TAG hydrothermal mound. *Geomicrobiology Journal*, 19(4), 429–438.

Amend, J., Rogers, K.L., Shock, E.L., Gurrieri, S., & Inguaggiato, S. (2003). Energetics of chemolithoautotrophy in the hydrothermal system of Vulcano Island, southern Italy. *Geobiology*, 1, 37–58.

Arancibia, O., & Clark, A. (1996). Early magnetite-amphibole-plagioclase alteration-mineralization in the Island copper porphyry copper-gold-molybdenum deposit, British Columbia. *Economic Geology*, 91, 402–438.

Awramik, S., Schopf, J., & Walter, M. (1983). Filamentous fossil bacteria from the Archean of Western Australia. *Precambrian Research*, 20(2-4), 357–374.

Bach, W., & Edwards, K.J. (2003). Iron and sulfide oxidation within the basaltic ocean crust: Implications for chemolithoautotrophic microbial biomass production. *Geochimica et Cosmochimica Acta*, 67(20), 3871–3887.

Bernet, M. (2005). Provenance Analysis by Single-Quartz-Grain SEM-CL/Optical Microscopy. *Journal of Sedimentary Research*, 75(3), 492–500.

Blackwelder, E. (1925). Exfoliation as a Phase of Rock Weathering. *Geology*, 33, 625–635.

Bogaerts, M., Scaillet, B., Liegeois, J., & Vander Auwera, J. (2003). Petrology and geochemistry of the Lyngdal granodiorite (Southern Norway) and the role of fractional crystallisation in the genesis of Proterozoic ferro-potassic A-type granites. *Precambrian Research*, 124(2-4),149–184.

Brack, A., & Pillinger, C.T. (1998). Life on Mars: chemical arguments and clues from Martian meterorites. *Extremophiles: life under extreme conditions*, 2(3), 313–319.

Braun J., Pagel, M., Herbillon, A., & Rosin, C. (1993). Mobilization and redistribution of REEs and thorium in a syenitic lateritic profile: A mass balance study. *Geochemica et Cosochimica Acta*, 51, 4419–4434.

Buick, R. (1990). Microfossil recognition in Archean rocks: an appraisal of spheroids and filaments from a 3500 my old chert-barite unit at North Pole, Western Australia. *Palaios*, 5(5), 441–459.

Cabral, A.R., Koglin, N., Seabra Gomes, A.A., & Lehmann, B. (2012). Xenotime-hematite aggregates on opaline filaments: evidence for biomineralization in weathered siliclastic rocks, Capanema, Quadrilatero Ferrifero of Minas Gerais, Brazil. *International Journal of Earth Sciences*, 101, 377–383.

Candela, P. (1997). A Review of Shallow, Ore-related Granites: Textures, Volatiles, and Ore Metals. *Journal of Petrology*, 38(12), 1619–1633.

Carr, M.J. (2002). IGPET for Windows. *Somerset, NJ: Terra Softa Inc.*

Chan, M.A., Bowen, B.B., & Parry, W.T. (2005). Red rocks and red planet diagenesis: Comparisons of Earth and Mars concretions, *GSA Today*, 15(8), 3-7.

Chang, S., & Kirschvink, J. (1989). Magnetofossils, the Magnetization of Sediments, and the Evolution of Magnetite Biomineralization. *Annual Review of Earth and Planetary Sciences*, 17, 169–195.

Davis, P. (1976). Interacting single-domain properties of magnetite intergrowths. *Journal of Geophysical Research*, 81(5), 989–994.

Deer, W., Howie, R. A., & Zussman, J. (2004). *Rock Forming Minerals. Volume 4B. Framework Silicates, Silica Minerals, Feldspathoids and Zeolites* (2nd ed. p. 958). Geological Society, London.

Dong, G., & Morrison, G. (1995). Adularia in epithermal veins, Queensland: morphology, structural state and origin. *Mineralium Deposita*, 30, 11–19.

Douka, C.E. (1977). Study of bacteria from manganese concretions. Precipitation of manganese by whole cells and cell-free extracts of isolated bacteria. *Soil Biology and Biochemistry*, 9(2), 89–97.

Edwards, K.J., Glazer, B.T., Rouxel, O.J., Bach, W., Emerson, D., Davis, R.E., Toner, B.M., Chan, C.S., Tebo, B.M., Staudigel, H., & Moyer, C.L. (2011). Ultra-diffuse hydrothermal venting supports Fe-oxidizing bacteria and massive umber deposition at 5000m off Hawaii. *The ISME Journal*, 5(11), 1748–1758.

Eggleton, R. (1985). The alteration of granitic biotite to chlorite. *American Mineralogist*, 70, 902–910.

Eickmann, B., Bach, W., Kiel, S., Reitner, J., & Peckmann, J. (2009). Evidence for cryptoendolithic life in Devonian pillow basalts of Variscan orogens, Germany. *Palaeogeography, Palaeoclimatology, Palaeoecology*, 283(3-4), 120–125.

Everitt, B.S., & Skrondal, A. (2010). *The Cambridge Dictionary of Statistics* (4th ed.). Cambridge University Press.

Ferris, F., Beveridge, T., & Fyfe, W. (1986). Iron-silica crystallite nucleation by bacteria in a geothermal sediment. *Nature*, 320, 609–611.

Forster, M., & Lister, G.S. (2003). Cretaceous metamorphic core complexes in the Otago Schist, New Zealand. *Australian Journal of Earth Sciences*, 50(2), 181–198.

Geological Association of Canada Mineral Deposits Division (GACMDD). (1996). *Atlas of Alteration* (p. 128). Mineral Deposit Research Unit.

Ghiorse, W.C., & Hirsch, P. (1982). Isolation and properties of ferromanganese-depositing budding bacteria from baltic sea ferromanganese concretions. *Applied and environmental microbiology*, 43(6), 1464–72.

Gibson, G., McDougall, I., & Ireland, T. (1988). Age constraints on metamorphism and the development of a metamorphic core complex in Fiordland, southern New Zealand. *Geology*, 16, 405–408.

Gibson, E.K., McKay, D.S., Thomas-Keprta, K.L., Wentworth, S.J., Westall, F., Steele, A., Romanek, C.S. Bell, M.S., & Toporski, J. (2001). Life on Mars: evaluation of the evidence within Martian meteorites ALH84001, Nakhla, and Shergotty. *Precambrian Research*, 106(1-2), 15–34.

Goldsmith, J., & Laves, F. (1954). The microcline-sanidine stability relations. *Geochimica et Cosmochimica Acta*, 5, 1–19.

Gustafson, L. (1975). The porphyry copper deposit at El Salvador, Chile. *Economic Geology*, 70, 857–912.

Hedenquist, J., & Lowenstern, J. (1994). The role of magmas in the formation of hydrothermal ore deposits. *Nature*, 370(18), 519–527.

Heider, F. (1987). Hydrothermal growth of magnetite crystals (1 m to 1 mm). *Journal of crystal growth*, 84, 50–56.

Heider, F., & Dunlop, D. (1987). Magnetic properties of hydrothermally recrystallized magnetite crystals. *Science*, 236(4806), 1287–1290.

Hein, J., Koschinsky, A., Halbach, P., Manheim, F.T., Bau, M., Kang, J., & Lubick, N. (1997). Iron and manganese oxide mineralization in the Pacific. *Manganese Mineralization: Geochemistry and Mineralogy of Terrestrial and Marine Deposits*. Geological Society Special Publication, 123–138.

Inoue, A. (1995). Formation of Clay Minerals in Hydrothermal Environments, *Origin and Mineralogy of Clays*. Springer, 268–329.

Ivarsson, M. (2006). Advantages of doubly polished thin sections for the study of microfossils in volcanic rock. *Geochemical transactions*, 7(1), 5.

Ivarsson, M., Lindblom, S., Broman, C., & Holm, N.G. (2008). Fossilized microorganisms associated with zeolite-carbonate interfaces in sub-seafloor hydrothermal environments. *Geobiology*, 6(2), 155–70.

Ivarsson, M., Broman, C., & Holm, N.G. (2011). Chromite oxidation by manganese oxides in subseafloor basalts and the presence of putative fossilized microorganisms. *Geochemical transactions*, 12(1), 5.

Jannasch, H.W., & Mottl, M.J. (1985). Geomicrobiology of deep-sea hydrothermal vents. *Science*, 229(4715), 717.

Juniper, S., & Fouquet, Y. (1988). Filamentous iron-silica deposits from modern and ancient hydrothermal sites. *The Canadian Mineralogist*, 859–869.

Kashefi, K., & Lovely, D. (2003). Extending the upper temperature limit for life. *Science*, 301(5635), 934.

Kirschvink, J., & Lowenstam, H. (1979). Mineralization and magnetization of chiton teeth: Paleomagnetic, sedimentologic, and biologic implications of organic magnetite. *Earth and Planetary Science Letters*, 44, 193–204.

Lowenstam, H. (1981). Minerals formed by organisms. *Science*, 211(4487), 1126–31.

Manhood, G., Nibler, G., & Halliday, A. (1996). Zoning patterns and petrologic processes in peraluminous magma chambers: Hall Canyon pluton, Panamint Mountains, California. *Geological Society of America Bulletin*, 108(4), 437–453.

Mann, S., Frankel, R.B., & Blackemore, R.P. (1984). Structure, morphology and crystal growth of bacterial magnetite. *Nature*, 4–5.

Martin, W.E., & Bils, R.F. (1964). Trematode Excretory Concretions: Formation and Fine Structure. *The Journal of Parasitology*, 50(3), 337–44.

Miyata. N., Tani, Y., Sakata, M., & Iwahori, K. (2007). Review: Microbial manganese oxide formation and interaction with toxic metal ions. *Journal of bioscience and bioengineering*, 104(1), 1–8.

Muir, R., Ireland, T.R., Weaver, S.D., Bradshaw, J.D., Waight, T.E., Jongens, R., & Eby, G.N. (1997). SHRIMP U-Pb geochronology of Cretaceous magmatism in northwest Nelson-Westland, South Island, New Zealand. *New Zealand Journal of Geology and Geophysics*, 40(4), 453–463.

Munha, J., Fyfe, W., & Kerrich, R. (1980). Adularia, the characteristic mineral of felsic spilites. *Contributions to Mineralogy and Petrology*, 75, 15–19.

Nathan, S. (1974). Petrology of the Berlins Porphyry: A Study of the Crystallisation of Granitic Magma. *Journal of the Royal Society of New Zealand*, 4(4), 463–483.

Nathan, S., Anderson, H.J., Cook, R.A., Herzer, R.H., Hoskins, R.H., Raine, J.I., & Smale, D. (1986). *Cretaceous and Cenozoic sedimentary basins of the West Coast Region, South Island, New Zealand*, New Zealand Geological Survey Basin Studies 1, Department of Scientific and Industrial Research.

Nathan, S., Rattenbury, M.S., & Suggate, R.P. (2002). Geology of the Greymouth area. Institute of Geological & Nuclear Sciences 1:250 000 geological map 12. 1 sheet + 58 p. Lower Hutt, New Zealand. Institute of Geological & Nuclear Sciences Limited.

Nesbitt, H.W., Markovics, G., & Price, R.C. (1980). Chemical processes affecting alkalis and alkaline earths during continental weathering. *Geochimica et Cosmochimica Acta*, 44, 1659–1666.

Ollier, C. (1971). Causes of spheroidal weathering. *Earth-Science Reviews*, 7, 127–141.

Palumbo. B., Bellanca, A., Neri, R., & Roe, M.J. (2001). Trace metal partitioning in Fe-Mn nodules from Sicilian soils, Italy. *Chemical Geology*, 173, 257–269.

Parry, W., & Downey, L. (1982). Geochemistry of hydrothermal chlorite replacing igneous biotite. *Clays and Clay Minerals*, 30(2), 81–90.

Peckmann, J., Bach, W., Behrens, K., & Reitner, J. (2008). Putative cryptoendolithic life in Devonian pillow basalt, Rheinishes Schiefergebirge, Germany. *Geobiology*, 6(2), 125–135.

Pedersen, K. (1997). Microbial life in deep granitic rock. *FEMS Microbiology Reviews*, 20(3-4), 399–44.

Pedersen, K. (2000). Exploration of deep intraterrestrial microbial life: current perspectives. *FEMS microbiology letters*, 185(1), 9–16.

Pye, K., Dickson, J.A.D., Schiavon, N., Coleman, M.L., & Cox, M. (1990). Formation of siderite-Mg-calcite-iron sulphate concretions in intertidal marsh and sandflat sediments, north Norfork, England. *Sedimentology*, 37(2), 325–343.

Raleigh, C. (1965). Crystallization and recrystallization of quartz in a simple piston-cylinder device. *The Journal of Geology*, 73(2), 369–377.

Rasmussen, B. (2000). Filamentous microfossils in a 3,235-million-year-old volcanogenic massive sulphide deposit. *Nature*, 405(6787), 676–679.

Roden, E.E., Sobolev, D., Glazer, B., & Luther, G.W. (2004). Potential for microscale bacterial Fe redox cycling at the aerobic-anaerobic interface. *Geomicrobiology Journal*, 21(6), 379–391.

Rong, X., Huang, Q., He, X., Chen, H., Cai, P., & Liang, W. (2008). Interaction of Pseudomonas putida with kaolinite and montmorillonite: A combination study by equilibrium adsorption, ITC, SEM and FTIR. *Colloids and Surfaces B: Biointerfaces*, 64, 49–55.

Røyne, A., Jamtveit, B., Mathiesen, J., & Malthe-Sorenssen, A. (2008). Controls on rock weathering rates by reaction-induced hierarchical fracturing. *Earth and Planetary Science Letters*, 275(3-4), 364–369.

Sahl, J.W., Schmidt, R., Swanner, E.D., Mandernack, K.W., Templeton, A.S., Kieft, T.L., Smith, R.L., Sanford, W.E., Callaghan, R.L., Mitton, J.B., & Spear, J.R. (2008). Subsurface microbial diversity in deep-granitic-fracture water in Colorado. *Applied and environmental microbiology*, 74(1), 143–52.

Schopf, J.W., & Walter, M.W. (1983). Archean microfossils: new evidence of ancient microbes, *Earth's Earlierst Biosphere, Its Origin and Evolution* Princeton university press, 214–239.

Sharp, Z. (2007). *Principles of Stable Isotope Geochemistry*, Pearson, Prentice Hall.

Shock, E.L. (1998). Slop98.dat, the upgraded thermodynamic database for the SUPCRT'92 Program. http:// http://geopig3.la.asu.edu

Sillitoe, R.H. (1972). A Plate Tectonic Model for the Origin of Porphyry Copper Deposits. *Economic Geology*, 67(2), 184–197.

Sillitoe, R. (2010). Porphyry copper systems. *Economic Geology*, 105, 3–41.

Sparks, N.H.C., Mann, S. Bazylinski, D.A., Lovley, D.R., Jannasch, H.W., & Frankel, R.B. (1990). Structure and morphology of magnetite anaerobically-produced by a marine magnetotactic bacterium and a dissimilatory iron-reducing bacterium. *Earth and Planetary Science Letters*, 98(1), 14–22.

Spell, T., McDougall, I. & Tullock, A. (2000). Thermochronological constraints on the breakup of the Pacific Gondwana margin: the Paparoa metamorphic core complex, South Island, New Zealand. *Tectonics*, 19, 433–451.

Staudigel, H., Furnes, H., McLoughlin, N., Banerjee, N.R., Connell, L.B., & Templeton, A. (2008). 3.5 billion years of glass bioalteration: Volcanic rocks as a basis for microbial life? *Earth-Science Reviews*, 89(3-4), 156–176.

Steiner, A. (1970). Genesis of hydrothermal K-feldspar (adularia) in an active geothermal environment at Wairakei, New Zealand. *Mineral. Mag*, 37(292), 916–922.

Stetter, K.O. (1999). Extremophiles and their adaptation to hot environments. *FEBS letters*, 452(1-2), 22–5.

Stipp, M., Stunitz, H., Heilbronner, R., & Schmid, S.M. (2002). The eastern Tonale fault zone: a "natural laboratory"for crystal plastic deformation of quartz over a temperature range from 250 to 700 C. *Journal of Structural Geology*, 24, 1861–1884.

Templeton, A.S., & Knowles, E. (2009). Microbial Transformations of Minerals and Metals: Recent Advances in Geomicrobiology Derived from Synchrotron-Based X-Ray Spectroscopy and X-Ray Microscopy. *Annual Review of Earth and Planetary Sciences*, 37(1), 367–391.

Templeton, A. S. (2011). Geomicrobiology of Iron in Extreme Environments. *Elements*, 7(2), 95–100.

Thorseth, I., Furnes, H & Heldal, M. (1992). The importance of microbiological activity in the alteration of natural basaltic glass. *Geochimica et Cosmochimica Acta*, 56(2), 845–850.

Thorseth, I., Torsvik, T., Torsvik, V., Daae, F.L., Pedersen, R.B., & Keldysh-98 Scientific Party. (2001). Diversity of life in ocean floor basalt. *Earth and Planetary Science Letters*, 194(1-2), 31–37.

Trewin, N.H. & Knoll, A.H. (1999). Preservation of Devonian chemotrophic filamentous bacteria in calcite veins. *Palaios*, 14(3), 288–294.

Uroz, S., Calvaruso, C., Turpault, M., & Frey-Klett, P. (2009). Mineral weathering by bacteria: ecology, actors and mechanisms. *Trends in microbiology*, 17(8), 378–387.

Waight, T. (1995). *The geology and geochemistry of the Hohonu Batholith and adjacent rocks, North Westland, New Zealand.* University of Canterbury.

Wandres A.M., Bradshaw J.D. (2005). New Zealand tectonostratigraphy and implications from conglomeratic rocks for the configuration of the SW Pacific margin of Gondwana. In *Terrane Processes at the Margins of Gondwana*. 179–216.

Wang, X., Schroder, H.C., Schlobmacher, U., & Muller, W.E.G. (2008). Organized bacterial assemlies in manganese nodules: evidence for a role of S-layers in metal deposition. *Geo-marine Letters*, 29(2), 85–91.

Wierzchos, J., Ascaso, C., Sancho, L.G., & Green, A. (2003). Iron-rich diagenetic minerals are biomarkers of microbial activity in Antarctic rocks. *Geomicrobiology*, 20, 37–41.

Winter, J. (2010). *Princliples of Igneous and Metamorphic Petrology* (2nd ed.), Pearson Education, Inc.

Xue, G., Qin, K., Li, X., Li, G., Qi, Z., & Zhou, N. (2012). Discover of a Large-scale Porphyry Molybdenum Deposit in Tibet through a Modified TEM Exploration Method. *Journal of Environmentail and Engineering Geophysics*, 17(1), 19–25.